



TechBriefs

National Aeronautics and
Space Administration



Electronic Components and Circuits



Electronic Systems



Physical Sciences



Materials



Computer Programs



Mechanics



Machinery



Fabrication Technology



Mathematics and Information Sciences



Life Sciences

INTRODUCTION

Tech Briefs are short announcements of new technology derived from the research and development activities of the National Aeronautics and Space Administration. These Briefs emphasize information considered likely to be transferable across industrial, regional, or disciplinary lines and are issued to encourage commercial application.

Availability of NASA Tech Briefs and TSP's

Distribution of NASA Tech Briefs, a monthly periodical publication, is limited to engineers in U.S. Industry and to other domestic technology transfer agents. Requests for individual Tech Briefs or for Technical Support Packages (TSP's) announced herein should be addressed to

NASA Center for AeroSpace Information
Technology Transfer Office
800 Elkridge Landing Rd.
Linthicum Heights, MD 21090-2934
Telephone No. (301) 621-0245

Please reference the three-letter, five-digit control number located at the end of each Tech Brief. Information on NASA's Technology Utilization Program, its documents, and services is also available at the same facility.

Technology Utilization Officers and Patent Counsels are located at NASA field installations to provide technology-transfer access to industrial users. Inquiries can be made by writing to NASA field installations listed below.

Technology Utilization Officers and Patent Counsels

Ames Research Center
Technology Utilization Officer
Mail Code 223-3
Moffett Field, CA 94035

Patent Counsel
Mail Code 200-11
Moffett Field, CA 94035

Goddard Space Flight Center
Technology Utilization Officer
Mail Code 702-1
Greenbelt, MD 20771

Patent Counsel
Mail Code 204
Greenbelt, MD 20771

Lyndon B. Johnson Space Center
Technology Utilization Officer
Mail Code IC-4
Houston, TX 77058

Patent Counsel
Mail Code AL3
Houston, TX 77058

John F. Kennedy Space Center
Technology Utilization Officer
Mail Stop PT-PMO-A
Kennedy Space Center, FL 32899

Patent Counsel
Mail Code PT-PAT
Kennedy Space Center, FL 32899

Langley Research Center
Technology Utilization Officer
Mail Stop 143
Hampton, VA 23665

Patent Counsel
Mail Code 279
Hampton, VA 23665

Lewis Research Center
Technology Utilization Officer
Mail Stop 7-3
21000 Brookpark Road
Cleveland, OH 44135

Patent Counsel
Mail Code LE-LAW
21000 Brookpark Road
Cleveland, OH 44135

Jet Propulsion Laboratory
Technology Utilization Officer
Mail Stop 156-211
4800 Oak Grove Drive
Pasadena, CA 91109

NASA Resident Office-JPL
Technology Utilization Officer
Mail Stop 180-801
4800 Oak Grove Drive
Pasadena, CA 91109

Patent Counsel
Mail Code 180-801
4800 Oak Grove Drive
Pasadena, CA 91109

George C. Marshall Space Flight Center
Technology Utilization Officer
Code AT01
Marshall Space Flight Center,
AL 35812

Patent Counsel
Mail Code CC01
Marshall Space Flight Center,
AL 35812

John C. Stennis Space Center
Technology Utilization Officer
Code HA-30
Stennis Space Center, MS 39529

NASA Headquarters
Technology Utilization Officer
Code CU
Washington, DC 20546

Assistant General Counsel for Patent Matters
Code GP
Washington, DC 20546

Dryden Flight Research Center
Technology Utilization Officer
M/S D21-31
Bldg. 4832 Whse 7
Lilly Dr.
Edwards, CA 93523



National Aeronautics and
Space Administration

TechBriefs

January 1996
96-01

5 Electronic Components and Circuits



15 Electronic Systems



21 Physical Sciences



31 Materials



35 Computer Programs



39 Mechanics



45 Machinery



49 Fabrication Technology



53 Mathematics and Information Sciences



FOR YOUR INFORMATION

This document was prepared under the sponsorship of the National Aeronautics and Space Administration. Neither the United States Government nor any person acting on behalf of the United States Government assumes any liability resulting from the use of the information contained in this document, or warrants that such use will be free from privately owned rights.

BLANK PAGE



Electronic Components and Circuits

Hardware, Techniques, and Processes

- 7 CMOS Active-Pixel Image Sensor With Intensity-Driven Readout
- 7 Lightweight Cathodes for Nickel Batteries
- 8 Megavolt, Multigigawatt Pulsed Plasma Switch
- 9 Ion-Accelerator Grids With Elongated Holes
- 10 High-Speed Binary-Output Image Sensor
- 10 Mode Orientation Control for Sapphire Dielectric Ring Resonator
- 11 Perforated-Layer Implementation of Radio-Frequency Lenses
- 12 Coding for Increased Density of Binary Data Stored on Disks
- 12 Hybrid-Circuit Module for dc-to-dc Power Converter
- 13 Thin-Ribbon Tapered Couplers for Dielectric Waveguides

2009 RELEASE

BLANK PAGE

CMOS Active-Pixel Image Sensor With Intensity-Driven Readout

Readings from pixels would be taken in order of decreasing intensity.

NASA's Jet Propulsion Laboratory,
Pasadena, California

A proposed complementary metal oxide/semiconductor (CMOS) integrated-circuit image sensor would automatically provide readouts from pixels in order of decreasing illumination intensity. Heretofore, no image sensor was capable of performing this function; the closest approximation to this function was provided by image sensors that gave the addresses of pixels above preset threshold levels.

The proposed image sensor could be operated in an integration mode. Its unique function would be particularly useful in a number of image-sensing tasks, including diffraction laser range-finding, three-dimensional imaging, event-driven readout of sparse sensor arrays, and star tracking. In these tasks, it is desirable to determine the location and intensity of the brightest pixel in an image as quickly as possible and to then read out the rest of the pixels in order of decreasing intensity for use in an integration mode.

The proposed image sensor (see Figure 1) would include a two-dimensional array of active pixel circuits, plus intensity-readout, winner-take-all, and address-encoder circuits. Acting together, these circuits would first select the address and the intensity reading of the brightest in the array, then repeatedly make a similar selection of the brightest pixel remaining after the previous selection.

A typical active pixel circuit in the proposed sensor (see Figure 2) would include a photodiode and four transistors. The photodiode would consist of a reverse-biased p^+ -doped region in an n -doped well. The diode would be connected to two n -channel gates in source followers connected to a common row and column line. The diode would also be connected to two n -channel transistors in series used to reset the pixel when selected.

After all pixels in the array (including this one) had been reset to 0 V, photocurrent

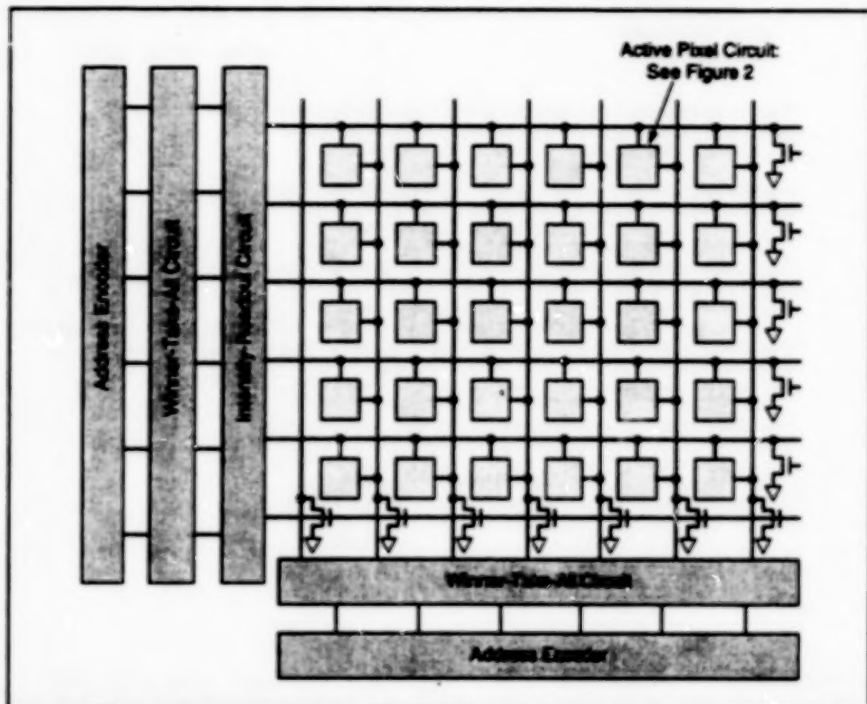


Figure 1. This CMOS Integrated-Circuit Image Sensor would provide readouts from pixels in order of decreasing intensity.

would charge the source-follower gates during an integration period, causing the source follower with the highest gate voltage to conduct while all others in the same row and column would be cut off. The winner-take-all circuits would select the column and row that intersect at the pixel with the greatest output (the winning pixel). The intensity reading and the encoded address of the winning pixel would be read out, and the winner-take-all circuits would enable the "select" signals to reset the winning pixel, removing it from the selection process. The foregoing functions would then be repeated until the intensity signals from a desired number of pixels had been read out.

This work was done by Harry T. Langenbacher, Eric R. Fossum, and Sabrina Kenney, of Caltech for NASA's Jet Propulsion Laboratory. Further

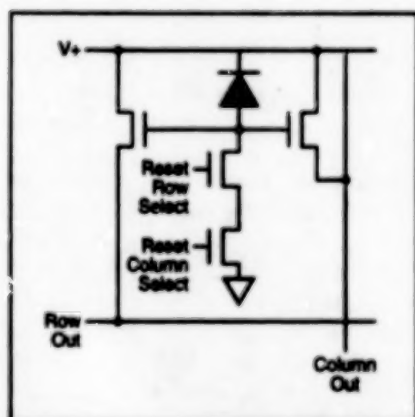


Figure 2. An Active-Pixel Circuit like this one would be located at the intersection of each row and column.

information is contained in a TSP [see page 1].
NPO-19539

Lightweight Cathodes for Nickel Batteries

Fibrous cathode mats accommodate more charge per unit mass.

Lewis Research Center,
Cleveland, Ohio

Lightweight cathodes for rechargeable nickel-based electrochemical cells are undergoing development. In these cathodes, mats of nickel fibers (instead of the sintered nickel plaques in older cathodes)

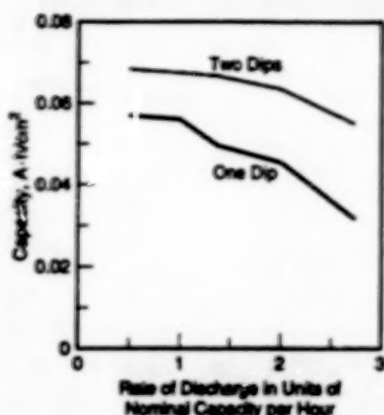
are the substrates that provide structural support of, and electrical contact with, the active cathode material. The fibrous nickel cathodes offer specific energies greater than those of sintered nickel

plaque cathodes; for example, a representative 48-A-h nickel/hydrogen cell made with a fibrous nickel cathode exhibits a specific energy of 90 Wh/kg, while the same cell made with a sintered

nickel plaque cathode exhibits a specific energy of 50 W-h/kg.

The fibrous cathodes could be used in a variety of nickel-based cell systems, including nickel/cadmium, nickel/zinc, nickel/metal hydride, and nickel/hydrogen. These electrodes are expected to be used in rechargeable batteries for applications in which weight is a major concern, including laptop computers, cellular phones, flashlights, soldiers' backpacks, and electric vehicles.

Like a sintered nickel cathode substrate, a fibrous nickel cathode substrate provides ample surface area for a coating with nickel hydroxide, which is the active electrode material. However, in comparison with a sintered substrate of the same capacity, a fibrous nickel substrate weighs less. Typically, the nickel fibers are 2 μ m in diameter. In fabrication of a cathode, a mat of nickel fibers is electrochemically impregnated with nickel hydroxide in an aqueous solution of 1.5 molar nickel nitrate, 0.175 molar cobalt nitrate, and 0.075 molar sodium nitrite at a current density of between 40 and 54 mA/cm² for an inter-



Two Dips in a solution of cobalt nitrate have been found to increase the capacity of a fibrous-nickel-substrate cathode even more than does a single dip.

val between 5 and 7 h at a temperature between 95 and 100 °C.

A 20-min postimpregnation dip in a solution of 1.8 molar cobalt nitrate increases the initial charge/discharge capacity of the cathode. The cathode is then subject-

ed to eight cycles of 20-min charge and 20-min discharge at a current density of 70 mA/cm² in a solution of 26 percent potassium hydroxide. This charge/discharge treatment removes impurities from the active cathode material and gives the active material the electrochemical analogue of exercise. After the eight charge/discharge cycles, the cathode is dipped again in cobalt nitrate solution to increase the capacity even more (see figure). Finally, the cathode is installed in a cell, along with a sintered nickel plaque anode, an asbestos separator between these two electrodes, and an electrolyte.

This work was done by Doris L. Britton of Lewis Research Center. Further information is contained in a TSP [see page 1].

Inquiries concerning rights for the commercial use of this invention should be addressed to the Patent Counsel, Lewis Research Center [see page 1]. Refer to LEW-15817.

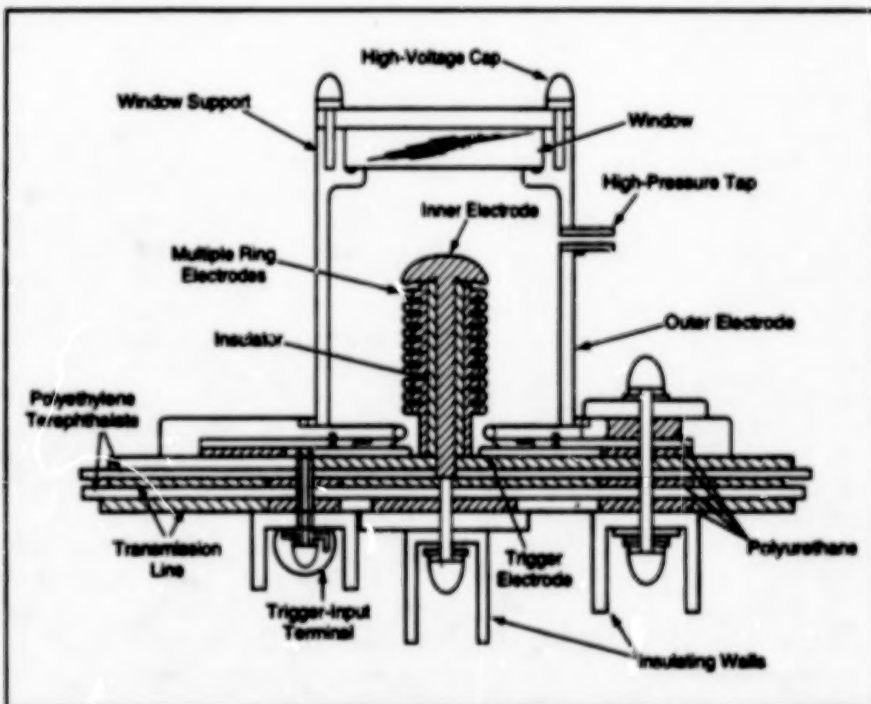
Megavolt, Multigigawatt Pulsed Plasma Switch

An inverse-pinch configuration would provide for dispersal of current over a relatively large area.

Langley Research Center,
Hampton, Virginia

The figure illustrates a plasma switch that has been proposed for use in a high-voltage, high-current pulse power system. The switch is required to hold off a potential of 1 MV when not triggered. The switch is required, when triggered, to transfer pulses with energies of 36 kJ apiece and durations of 1 μ s (corresponding to a peak power of about 36 GW) at a repetition frequency of 10 Hz from a pulse-forming transmission line that has an impedance of 2 Ω . This severe combination of requirements can be satisfied only by a spark-gap switch near the upper limit of its performance. The proposed switch would be a spark-gap switch but would differ radically from conventional spark-gap switches. It has been designed not only to outperform a conventional spark-gap switch but also to be relatively compact and lightweight.

Flat-plate input and output transmission lines would be connected to the switch and would be immersed in oil to satisfy high-voltage and impedance-matching requirements. The main current-carrying electrodes would be (1) an outer electrode shaped like a cylindrical cup with a hole in the bottom and (2) a mushroom-shaped inner electrode surrounded by (3) an insulator and a skirt of



The Plasma Switch would feature an inverse-pinch configuration to prevent constriction of current sheets into filaments, plus a multiple-ring-electrode structure to resist high-voltage breakdown.

multiple ring electrodes separated by uniform gaps. This multiple-ring-electrode configuration would serve, in conjunction with pressurized SF₆ dielectric gas, to

resist electrical breakdown and thereby satisfy the 1-MV hold-off requirement. The dimensions of the electrodes are chosen, not only with regard to the hold-off

requirement, but also to minimize the inductance and capacitance of the switch to achieve high switching speed (rise time required to be $< 0.1 \mu\text{s}$).

A discharge would be triggered by use of a trigger electrode located at the base of the outer electrode. A high-voltage trigger pulse would be fed to the trigger electrode, causing a flashover on an adjacent ceramic disk insulator. This would generate a plasma ring, which would puff up axially toward the lowest ring electrode, where it would initiate breakdown current from the outer to the

inner electrode via the multiple ring electrodes; the gaps in series in the multiple-ring-electrode structure would break down simultaneously because of over-voltage caused by plasma closing of the lowest gap.

The switch is designed in an inverse-pinch configuration, which has been used in other plasma devices, but not in spark-gap switches. In the inverse-pinch configuration, the electrode and insulator surfaces are arranged so that the ponderomotive force of the current upon itself would act to sweep the current sheet

radially outward and axially upward from its initial discharge path along the multiple-ring-electrode structure. Thus, once a discharge was triggered, the current would sweep over the broad electrode surfaces instead of constricting the current sheet into filaments that cause hot spots, as in conventional spark gaps.

This work was done by Ja H. Lee of Langley Research Center and Sang H. Choi and Kyo D. Song of Source Tek, Inc. Further information is contained in a TSP [see page 1].
LAR-14422

Ion-Accelerator Grids With Elongated Holes

Grids are stronger and costs of fabrication lower than for grids with circular holes.

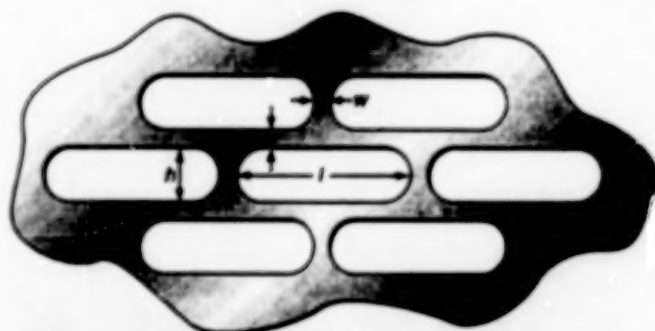
NASA's Jet Propulsion Laboratory,
Pasadena, California

Ion-accelerator grids have been designed and fabricated with elongated holes instead of the circular holes used heretofore. Although the grids are made of lightweight carbon/carbon composites and were conceived for use in ion thrusters for spacecraft, they could also be made of other materials and installed in industrial ion accelerators for material-processing applications. In comparison with circular holes, the elongated holes offer advantages of lower costs of fabrication and the option to increase the open-area fractions of the grids, thereby increasing the output ion currents that can be extracted through the grids.

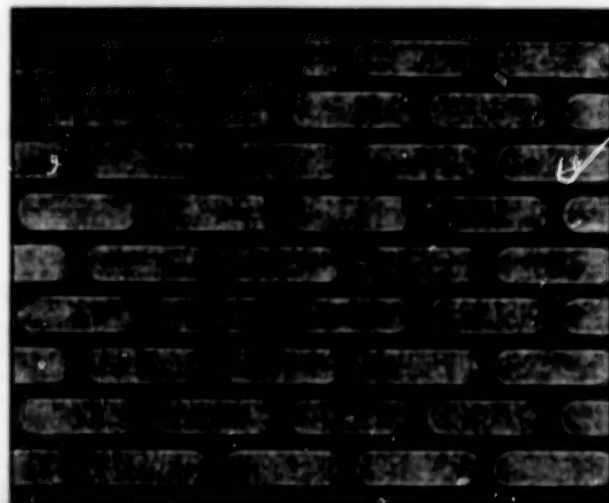
As shown in the upper part of the figure, each hole has a length l and consists of a rectangular center section of width h with semicircular end segments. Adjacent holes are separated by a web of thickness w . The dimensions l , h , and w can be varied to obtain a specified open-area fraction and to obtain a specified number of holes in a grid of a specified diameter. Fewer elongated holes are needed to obtain the same open-area fraction as that provided by circular holes of a given diameter and spacing.

Typically, the holes are cut one at a time by electrical-discharge machining, which takes the same amount of time to make an elongated hole as to make a circular hole. Thus, an elongated-hole design offers the opportunity to reduce fabrication time and cost in approximate proportion to the reduction in the number of holes relative to a circular-hole design.

The following example illustrates the advantages of the elongated-hole concept. A state-of-the-art ion-engine grid of 15-cm diameter contains approximately 4,500 circular holes, with an open-area



ELONGATED HOLE PATTERN



PHOTOGRAPH OF ELONGATED HOLES IN A CARBON/CARBON COMPOSITE GRID

Elongated Holes can be designed to provide open-area fractions equal to or greater than those of circular holes.

fraction of 67 percent. The diameter of the holes is about 1.9 mm, and the thicknesses of the webs between holes can be as little as 0.3 mm. These dimensions impose severe design requirements and make fabrication expensive. The same open-area fraction can be achieved with

only 1,100 elongated holes like those shown in the lower part of the figure, for which $l = 6.35 \text{ mm}$, $h = 1.9 \text{ mm}$, and $w = 0.56 \text{ mm}$. Thus the same open-area fraction can be maintained with a webbing thickness almost twice as large as for the circular holes. Therefore, a grid

using an elongated hole design is stronger and easier to fabricate than one using a circular hole design because the webs are thicker. The number of elongated holes being slightly less than 1/4 the number of circular holes, machining of

the elongated holes should cost only about 1/4 as much.

In cases in which smaller w can be tolerated, open-area fractions could be increased, with corresponding increases in output currents.

This work was done by Juergen Mueller of Caltech for NASA's Jet Propulsion Laboratory. Further information is contained in a TSP [see page 1].
NPO-19336

High-Speed Binary-Output Image Sensor

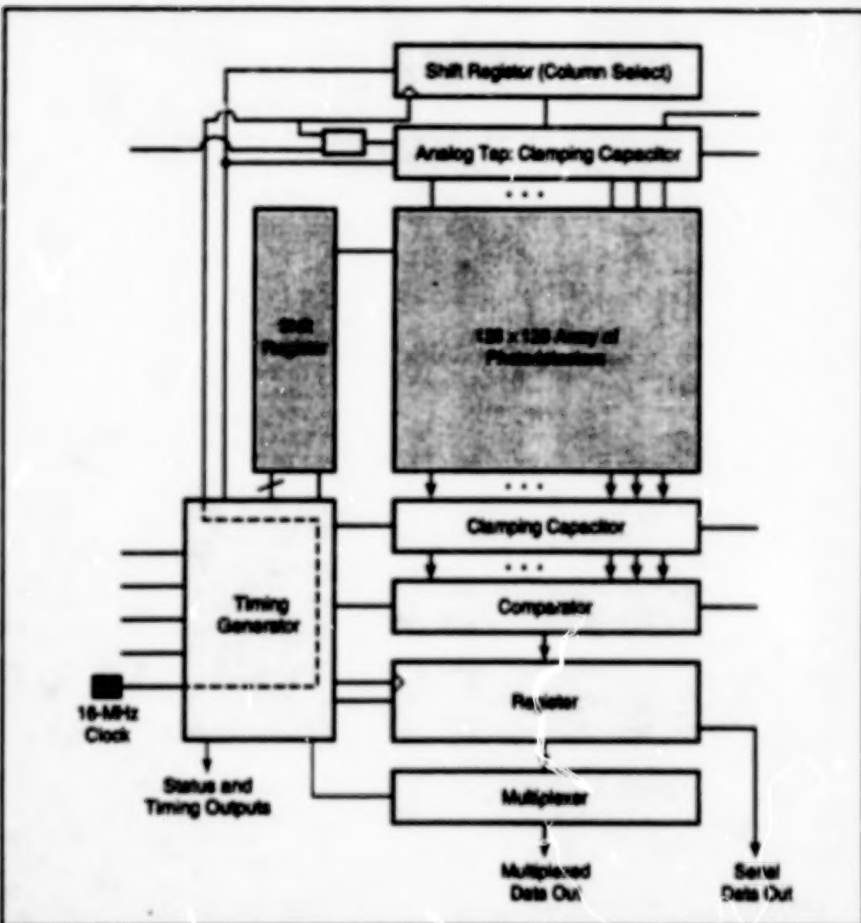
Photodetector outputs are digitized by circuitry on the same integrated-circuit chip.

NASA's Jet Propulsion Laboratory,
Pasadena, California

A developmental special-purpose binary-output image sensor is designed to capture up to 1,000 images per second, with a resolution greater than 10^6 pixels ($1,024 \times 1,024$ to be precise) per image. A lower-resolution but higher-frame-rate (8,000 images per second) prototype of the sensor contains a 128×128 array of photodiodes on a complementary metal oxide/semiconductor (CMOS) integrated-circuit chip. In the special application for which it is being developed, this sensor would be used to examine helicopter oil to determine whether the amount of metal and sand in the oil is sufficient to warrant replacement. In this application, pulsed laser light at a wavelength of 850 nm would be directed through a sample of oil and onto the array of photodiodes.

The figure illustrates the major functional blocks of the sensor. During operation, the photodiodes are reverse-biased, and are partially discharged, from their reset voltage, by photogenerated electrons. In response to timing and control signals, a row shift register reflects the current row of pixels (photodiodes). An active in-pixel source-follower buffers the photodiode voltage and drives the column line. Circuitry on all 128 columns detects the resulting changes in the voltages across the photodiodes at the selected row/column intersections. A digital "1" or "0" is produced by comparator circuitry for each column, depending on whether the pixel signal in question is above or below an externally set threshold level. Either 1-bit or 2-bit representations of the analog signals can be obtained.

The resulting binary data signals for all columns in the current row are loaded in parallel into a register, for output in either of



This Image-Sensing Integrated-Circuit Chip generates most of its internal control and timing signal from an externally supplied 16-MHz clock signal. The chip also produces chip-status and frame-timing signals. The short lines at the right and left sides of the figure indicate various control and bias connections.

two formats. In one higher-speed format, the data are available as a serial stream of 16 Mb/s; in the other format, the data are multiplexed at a width of 8 bits at a clock rate of 16 MHz for a 128 Mb/s effective data rate.

This work was done by Eric Fossum, Roger A. Penicucci, Sabrina E. Kerny, and Peter D. Jones of Caltech for NASA's Jet Propulsion Laboratory. Further information is contained in a TSP [see page 1].
NPO-19520

Mode Orientation Control for Sapphire Dielectric Ring Resonator

A tuning wedge breaks a quasi-degeneracy of two modes and allows selective coupling to just one mode.

NASA's Jet Propulsion Laboratory,
Pasadena, California

A small sapphire tuning wedge is used in a technique for solving a mode-purity problem associated with a sap-

phire dielectric-ring resonator that is part of a cryogenic microwave frequency discriminator. Such a resonator is typically

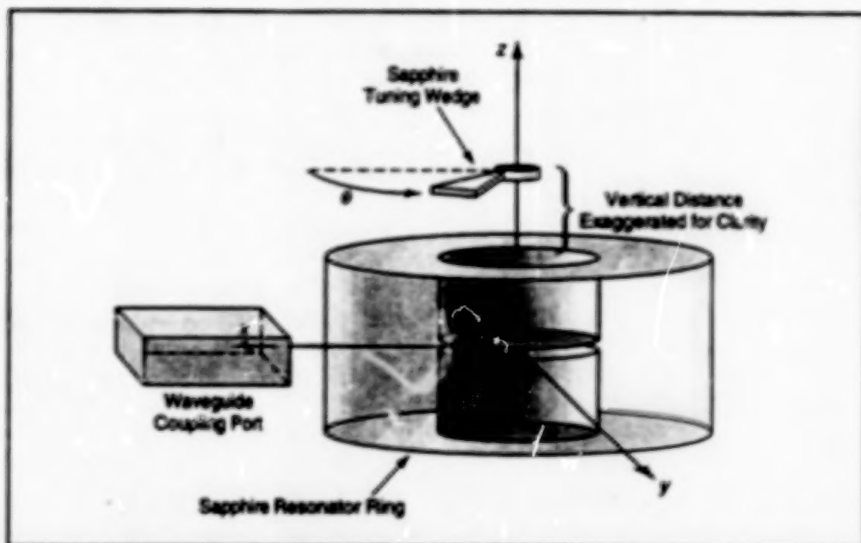
used to stabilize the frequency and ensure the spectral purity of a microwave signal generated by frequen-

cy multiplication from a 5-MHz quartz-crystal oscillator.

The mode-purity problem can be summarized as follows: The resonator supports whispering-gallery electromagnetic modes, which present mode degeneracies common to any circularly symmetric waveguide. Because of small geometrical imperfections that are difficult to identify, the sapphire cavity resonates in a pair of quasi-degenerate modes split by a few kHz. The random angular orientation of these modes results in uncontrolled coupling of the modes to a fixed waveguide port, whereas selective coupling of one of these modes to the port is required.

The mode orientation can be controlled by adding a perturbation that is greater than that of the geometric imperfections. In the present technique, the perturbation is added by installing a sapphire tuning wedge above the sapphire ring (see figure).

The sapphire tuning wedge changes the configuration of the dielectric medium that supports standing waves outside the resonator. The dielectric perturbation introduced by the tuning wedge becomes the dominant effect that determines the circumferential alignment of the modes with respect to the waveguide coupling port. Thus, by rotating this tuning wedge, one can rotate the resonant standing-wave pattern with respect to the port to obtain



The Small Sapphire Tuning Wedge above the sapphire resonator ring introduces a dominant perturbation that breaks a mode degeneracy and controls angular orientation of the modes. Selective coupling to just one mode is obtained by turning the wedge to the desired angle, θ ; the frequency is adjusted by moving the wedge to the desired height, z .

coupling to only the desired mode. In addition to providing coupling control, the tuning wedge increases the frequency separation between the two quasi-degenerate modes to about 56 kHz—a feature that further reduces coupling to the undesired mode. The tuning wedge can be mounted on an axis that enters the resonator cavity and can be rotated while the resonator is cryogenically operating in a vacuum. Furthermore, the axis can also be

moved vertically to tune the resonant frequency.

This work was done by David G. Santiago and G. John Dick of Caltech, and Aluizio Prata of the University of Southern California for NASA's Jet Propulsion Laboratory. Further information is contained in a TSP [see page 1], NPO-18933.

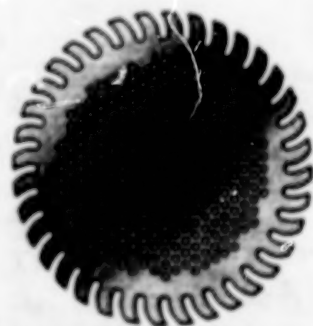
Perforated-Layer Implementation of Radio-Frequency Lenses

The perforation pattern would be designed to achieve the required spatial variation of permittivity.

NASA's Jet Propulsion Laboratory,
Pasadena, California

Luneberg-type radio-frequency dielectric lenses would be made of stacked perforated circular dielectric sheets, according to a proposal. (A Luneberg lens is a dielectric sphere, the index of refraction of which varies with distance from the center such that a beam of parallel rays incident on one face of the sphere is focused to a point on the opposite face.) The perforations would consist of round holes distributed across the face of each sheet in a "Swiss-cheese" pattern, plus straight or curved slots that would break up the outer parts into petals in a "daisy-wheel" pattern (see figure). The holes and slots would be made by numerically controlled machining.

The basic idea is to choose the distribution of holes and slots such that at any given location within the lens, the effective local relative permittivity ϵ_{eff} equals the square of the index of refraction prescribed by the Luneberg-lens formula. The requirement is expressed



SECTION A-A, SHOWING ONE LAYER

Circular Layers of Dielectric Material containing holes and slots would be assembled and bonded together to form a spherical dielectric lens. To save machining time, multiple sheets with identical patterns of holes and slots (e.g., sheets at the same latitude in both hemispheres) could be machined together.

by $\epsilon_{eff} = 2 - [(h^2 + r^2)^{1/2} / R]$, where R is the radius of the sphere, h is the distance (along the optical axis) of the layer in question from the center of the sphere, and r is the distance of the location in

question from the center of the layer (equivalently, the lateral distance from the optical axis).

For the purpose of this concept, ϵ_{eff} is considered to be the volume-average

permittivity in a small neighborhood around the location of interest and is given by $\epsilon_{eff} = (\epsilon_m - 1)(1 - v) + 1$, where ϵ_m is the relative permittivity of the dielectric material and v is the local volume fraction of holes and slots. The distribution of the volume fraction of holes and slots that yields the required distribution of ϵ_{eff} is given by $v = (\epsilon_m - 2 + [(\epsilon_m - 2)^2 + 4R]) / (\epsilon_m - 1)$.

Of course, the validity of this concept depends on the use of a sufficient number of holes and/or slots to justify a volume average. Furthermore, each hole or slot must be much smaller than a wavelength at the radio frequency of interest

so that no single one significantly affects the propagation of the electromagnetic waves passing through it.

The patterns of holes and slots must satisfy some additional practical requirements: When the layers are stacked, there must be no sealed pockets in which pressurized gas could be trapped. The holes and slots in adjacent layers must not be concentric with or parallel to each other, respectively, or else they could effectively form larger holes and slots that could affect propagation to an unacceptable degree. The patterns must also be chosen to minimize the cost of

machining; for example, the number of different drill sizes should be minimized.

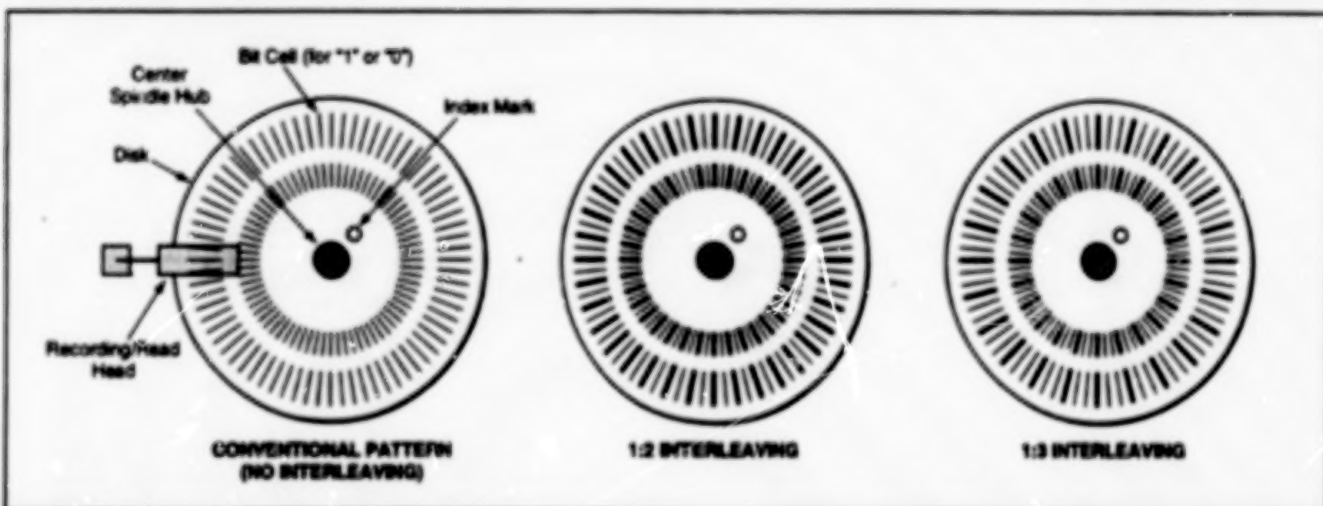
In stacking the perforated layers to assemble a lens, the holes could be used as alignment surfaces. The layers would preferably be bonded together by ultrasonic welding; adhesive bonding would not be acceptable because it would introduce solvents that could affect dielectric properties.

This work was done by Benjamin P. Dognin of Caltech for NASA's Jet Propulsion Laboratory. Further information is contained in a TSP [see page 1], NPO-19217

Coding for Increased Density of Binary Data Stored on Disks

Interleaved bit patterns provide for bit density with low readout rates.

NASA's Jet Propulsion Laboratory,
Pasadena, California



Data Would Be Stored in Interleaved Patterns Instead of the conventional noninterleaved pattern of sequential bits in adjacent cells. For the sake of clarity, only two tracks are shown, with the numbers of bit cells greatly reduced. In the interleaved patterns, each bit cell shown in bold is logically (sequentially) related to the next bit cell shown in bold.

Interleaved bit patterns have been proposed as the basis of a scheme for increasing the density of binary data stored on disks. Unlike in some other schemes for increasing data-storage density, the readout rate would not necessarily have to increase proportionally to the density and thus there may not be a need for correspondingly faster readout circuitry.

The bit densities of computer data-storage disks are increased to increase overall data-storage capacities. To enable rapid

access to data stored on the disks, the speeds of rotation of the disks are also increased. With increases in both bit density and disk speed, the rates at which data flow to and from disks increase. These data rates can become too high for cost-effective electronics to handle.

The proposed interleaved bit patterns would contain bits at high density, except that the bits written in adjacent bit cells would belong to different sequences, and the bits in any given sequence would be

written at intervals of N bit cells, where N denotes the depth of interleaving (see figure). Thus, the data in any given sequence would be read out at a rate equal to the readout rate for data stored at $1/N$ of the actual high density.

This work was done by Romney R. Kati of Caltech for NASA's Jet Propulsion Laboratory. Further information is contained in a TSP [see page 1], NPO-19036

Hybrid-Circuit Module for dc-to-dc Power Converter

External components determine output voltage and provide dc isolation.

A small, high-efficiency hybrid module is designed to provide many of the functions of a dc-to-dc, dc-isolating power converter. This is a general-purpose

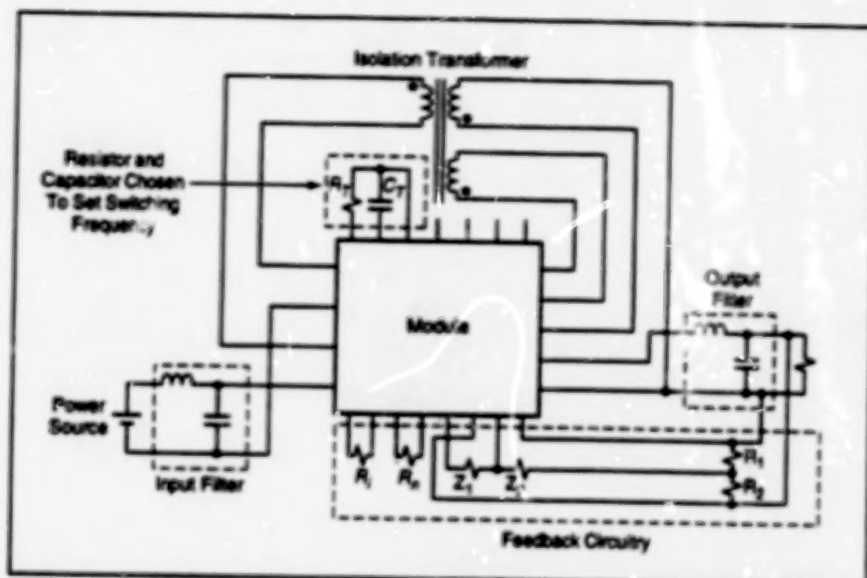
module that contains all of the power- and signal-switching and analog signal-processing circuits that are likely to be needed. A circuit designer can add input

NASA's Jet Propulsion Laboratory,
Pasadena, California

and output filters, an isolation transformer, and a feedback compensation network (see figure) to obtain a complete dc-to-dc power converter.

A power converter that incorporates this module can operate at a maximum input voltage of 50 V. The output can be adjusted from 2.5 to 12 V. A 5-V (0- to 6-A) converter, switching at 50 kHz, with a 23- to 35-V input bus, has a maximum efficiency of 92 percent. Switching frequency can be adjusted up to several hundred kHz by the choice of R_T and C_T . Alternatively, the switching can be synchronized with an externally generated clock signal. If an isolation transformer with additional secondary windings is provided, multiple slave outputs can be obtained.

This work was done by Vatche Vorperian, Robert Detwiler, and Dan Karmon of Caltech for NASA's Jet Propulsion Laboratory. Further information is contained in a TSP [see page 1], NPO-19411.



The Power Hybrid Module is a general-purpose power-switching module that provides flexibility in design and application. A complete dc-to-dc power converter can be constructed by adding the input/output filters and feedback circuitry to this module to suit the specific application.

Thin-Ribbon Tapered Couplers for Dielectric Waveguides

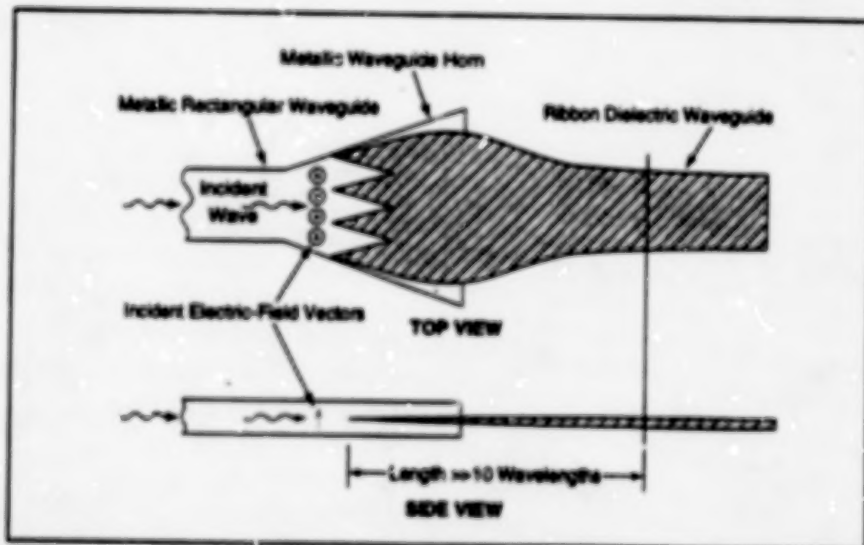
Coupling efficiencies would exceed those of older tapered couplers.

NASA's Jet Propulsion Laboratory,
Pasadena, California

Thin-ribbon tapered couplers have been proposed for launching electromagnetic waves into dielectric waveguides, which could include optical fibers. These couplers are intended especially for use with ribbon dielectric waveguides that are (1) designed for operation at millimeter or submillimeter wavelengths, (2) made of high-relative-permittivity, low-loss materials (e.g., TiO_2 , with relative permittivity of 100 and loss tangent of 2.5×10^{-6}), and (3) have thicknesses comparable to or less than the free-space design wavelengths.

These tapered couplers would offer coupling efficiencies greater than those of couplers that were designed according to the older concept of tapering the coupling end of a dielectric waveguide down to a single, sharp apex. For ribbon dielectric waveguides, this older concept is not practical when a material has a relative permittivity $\gg 1$. This is because in the case of such a high relative permittivity, the cross-sectional dimensions of the taper must be made very small to achieve good impedance matching between the dielectric waveguide and free space. This requirement, in turn, makes it difficult to handle and align the taper.

Moreover, the stability of those mode(s) of the electromagnetic field that adhere to the taper becomes questionable. In other words, it is difficult to excite a guided



The End of a Dielectric Waveguide Would Be Tapered to a wide, thin, flattened section to enhance coupling of electromagnetic waves from a metal waveguide (or from free space).

wave along the tapered section of a high-relative-permittivity dielectric waveguide, even when good impedance matching is present. It appears that the surface area of the tapered section is too small for efficient capture of the incident wave and transformation of the incident wave into a guided wave.

A thin-ribbon tapered coupler according to the present concept would be formed by forming a dielectric waveguide into a wide, thin, flattened section. Typically, waves would be launched into the dielec-

tric waveguide from a metal waveguide with an end taper fitted to that of the dielectric waveguide. Optionally, the transition region could be extended by use of a comblike structure at the end (see figure). The dimensions of the dielectric waveguide and its coupling taper would be chosen to obtain the required impedance match and coupling efficiency; for this purpose, the propagation of waves and conversion modes would be analyzed by use of conventional waveguide mode equations with some simplifying assumptions.

Because of its large surface area, the dielectric taper could easily be supported mechanically without noticeable perturbation of the electromagnetic field. In comparison with a narrow taper of the older type, this taper would feature a much

larger surface area, which would enable the guided surface wave to attach itself better to the waveguide, thereby increasing the launching efficiency.

This work was done by Tom Y. Otoshi, Fred I. Shimabukuro, and Gavour Yeh of

Caltech for NASA's Jet Propulsion Laboratory. Further information is contained in a TSP [see page 1].
NPO-19296



Electronic Systems

Hardware, Techniques, and Processes

- 17 Automatic Phase-Compensation Modules for Antennas
- 18 Advanced Triangulation Displacement Sensors
- 19 Measuring Motor-Shaft Clearance and Wobble During Operation

BLANK PAGE

Automatic Phase-Compensation Modules for Antennas

The modules would be used to correct for distortions in antenna reflectors.

Lewis Research Center,
Cleveland, Ohio

Automatic amplitude-controlling and phase-shifting modules are being developed in order to adaptively compensate for distortions in the reflectors of microwave communication antennas. An antenna of the type in question would include a phased array of radiating antenna elements in the focal plane of an off-axis paraboloidal or similar reflector. A module of the type in question would lie on the path of the radio-frequency feed between each antenna element and the radio-frequency transmitting/receiving equipment (see Figure 1).

The objective of the compensation scheme is to make the transmitted far field closely approximate a plane wave, despite deviations of the reflector from the ideal paraboloidal or other design figure. First, the antenna would be made to receive a plane wave by aiming it at a distant radio source of the desired frequency. The amplitude and phase of the signal received by each element would be measured. Inasmuch as this amplitude and phase would be that associated with the actual received electromagnetic field, it would necessarily include a measure of the electromagnetic effects of distortion in the reflector.

A control computer associated with the phased array would use the phases and amplitudes measured during reception to compute the excitations to be supplied to the antenna elements during subsequent transmission. The computed excitations would compensate for the distortions in the reflector on the basis of the principle of direct conjugate field matching. According to this principle, the excitation that must be supplied to each element to obtain a transmitted far field that approximates a plane wave has a complex amplitude proportional to the complex conjugate of signal measured at that element during reception.

Each automatic amplitude-controlling and phase-shifting module would include an automatic phase-conjugation submodule that would measure the amplitude and phase of the signal received by its antenna element. Figure 2 is a block diagram of a prototype submodule that has been built and tested. The submodule includes a phase shifter that is used to adjust the phase of the excitation during transmission. During reception, the phase shift is set to zero

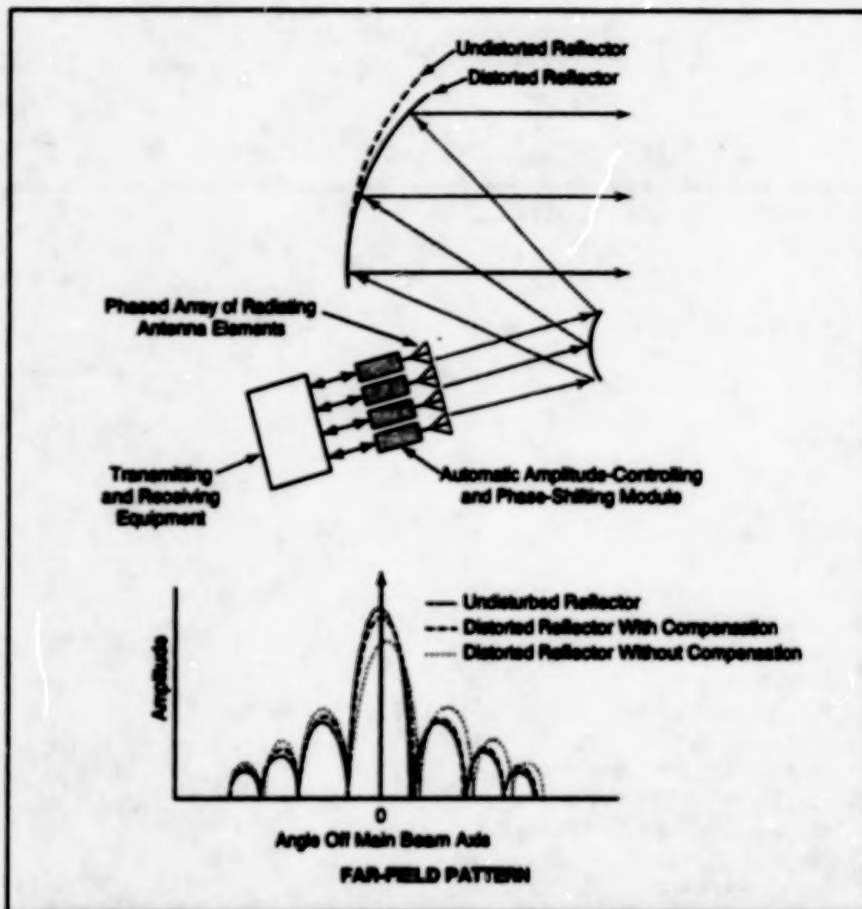


Figure 1. Automatic Amplitude-Controlling and Phase-Shifting modules in the phased array of radiating elements would compensate for distortions in the reflector to obtain an approximation of the desired far radiation field.

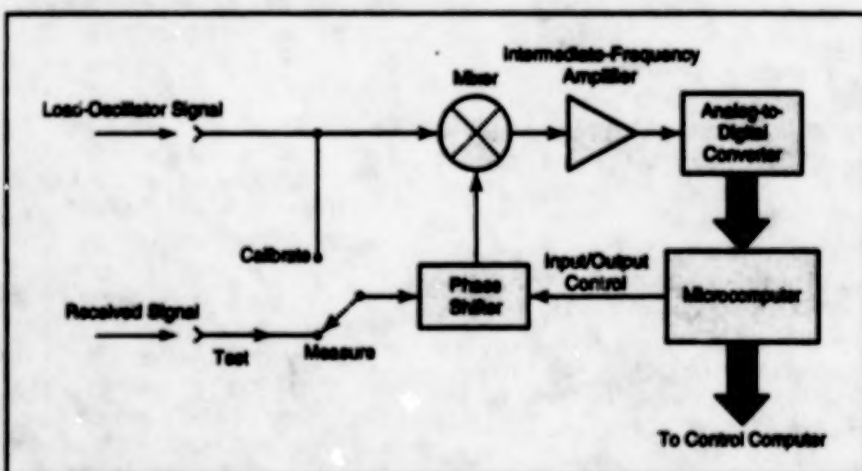


Figure 2. This Automatic Phase-Conjugation Submodule is a prototype of identical units that would be incorporated into the automatic amplitude-controlling and phase-shifting modules of Figure 1.

and the received signal is mixed with a local-oscillator signal to shift the received signal to an intermediate frequency (IF). The IF signal is amplified,

then digitized at a sampling rate equal to a multiple of the IF.

A microcomputer multiplies the digital IF received-signal samples by digital samples of

in-phase and quadrature versions of a synchronizing IF sinusoid that is supplied in common to all the modules. The microcomputer performs discrete-product integrations by summing the products of these multiplications. The results of the discrete-product integrations are an in-phase component (ρ) and a quadrature component (ρ_Q) propor-

tional to those of the received signal. The phase (θ) of the received signal is then computed from $\theta = \tan^{-1}(\rho_Q/\rho)$ and a number (I) proportional to the amplitude of the received signal is computed from $I = (\rho^2 + \rho_Q^2)^{1/2}$. Applying the principle of direct conjugate field matching, the amplitude of the signal supplied to the radiating element during subse-

quent transmission would be adjusted to be proportional to I , while the phase of the signal would be shifted by the amount of $-\theta$.

This work was done by John D. Terry and Richard R. Kunath, Jr., of Lewis Research Center. Further information is contained in a TSP [see page 1].
LEW-15719

Advanced Triangulation Displacement Sensors

Measurements are expected to be accurate to within nanometers.

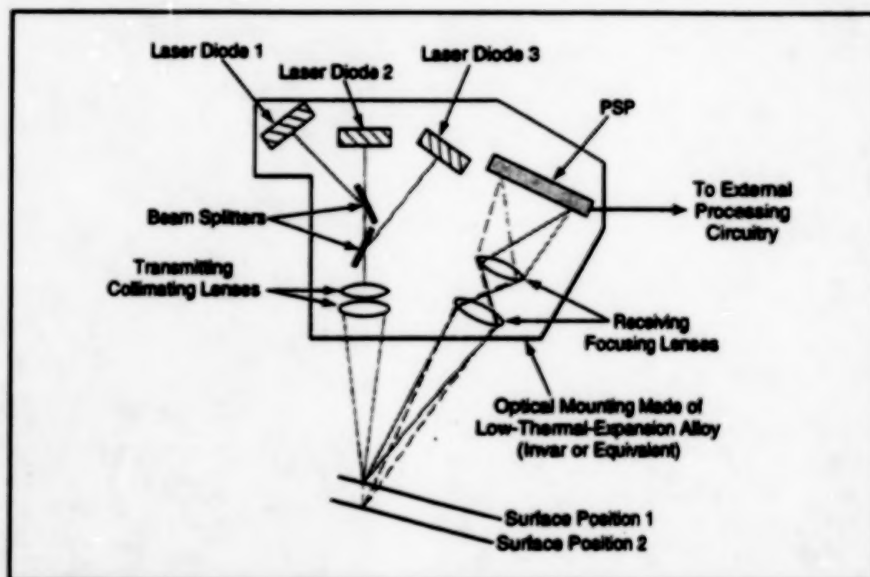
Marshall Space Flight Center,
Alabama

Advanced optoelectronic triangulation displacement sensors are undergoing development. In comparison with other optoelectronic triangulation displacement sensors, these are highly miniaturized, more stable, more accurate, and relatively easy to use. Moreover, these sensors incorporate wide-band (frequency response up to 10 kHz) electronic circuits that are suitable for real-time monitoring and control of displacements. In principle, these sensors could be mass-produced at relatively low unit cost.

A typical sensor of this type (see figure) contains as many as three laser diodes for generating beams of light to be used in triangulation. Beam splitters combine the three laser beams, then transmitting lenses collimate the combination beam into a narrow beam that makes a small spot of light on the surface, the displacement of which is to be measured. Light reflected from the surface at the spot is intercepted by receiving lenses, which focus the light to a small spot on a position-sensitive photodetector (PSP). By the basic principle of triangulation, the position of the spot of light on the PSP is related in a known way to the distance from the sensor to the spot of light on the surface.

The lenses are fabricated, variously, as binary and/or gradient-index optics; they feature precise optical designs that correct for astigmatism and provide light-spot sizes that range from 1 μ m to 1 mm, depending on the required fineness or coarseness of detail required. With suitable design of the lenses, spatial filtering of the transmitted and reflected beams of light, and the choice of a super-linear-response PSP, it should be possible to measure the sensor-to-surface distance to within 2 nm.

The analog output of the PSP is amplified, conditioned, and digitized for processing by external circuitry. It should be



An Advanced Triangulation Sensor is typically 1/100 to 1/10 the size of triangulation sensors that have been used until now.

noted that changes in the finish and/or color of the surface in question do not affect accuracy to first order, because it is the position, rather than the intensity or color of the spot of light that is measured. Digital processing of the output includes corrections for nonlinearities in the response of the PSP and for the effects of variations of temperature. These corrections are obtained initially by taking calibration measurements, and are stored in firmware (a programmable read-only memory that is part of the digital processing circuitry).

The reason for including more than one laser diode is that by performing triangulation measurements at more than one wavelength and using the known values of the index of refraction of a transparent or semitransparent surface layer at those wavelengths, one can measure not only the distance to the surface but also the thickness of the surface layer. For this purpose, the outputs of the laser diodes are modulated at different phases, so that the corresponding PSP outputs can

be processed in synchronism to obtain the triangulation data for the different wavelengths.

Potential applications for these advanced triangulation sensors are numerous. For example, the surface of a precise mirror undergoing fabrication can be measured directly to better than 1/12 of a wavelength of 830 nm by scanning such a sensor over the surface, using the same mounting structure that has been used to generate and polish the mirror surface. Semiconductor wafers can be measured before and after processing to measure stress-induced warp and bow. Because of their wideband electrical characteristics, these sensors could be used as real-time position sensors or precise feedback control of scanning, chopping, and focusing motions of optical components, including focusing of secondary mirrors of astronomical telescopes. A possible industrial application might lie in measuring runout of a rotating shaft or other moving part during fabrication in a "zero-

defect" manufacturing system, in which the measured runout is automatically corrected.

This work was done by Wade M. Poteet and Harold K. Cauthen of System

Specialists, Inc., for Marshall Space Flight Center. Further information is contained in a TSP [see page 1].

Inquiries concerning rights for the commercial use of this invention should be

addressed to the Patent Counsel, Marshall Space Flight Center [see page 1]. Refer to MFS-26324.

Measuring Motor-Shaft Clearance and Wobble During Operation

The rate of rotation can also be measured.

Goddard Space Flight Center, Greenbelt, Maryland

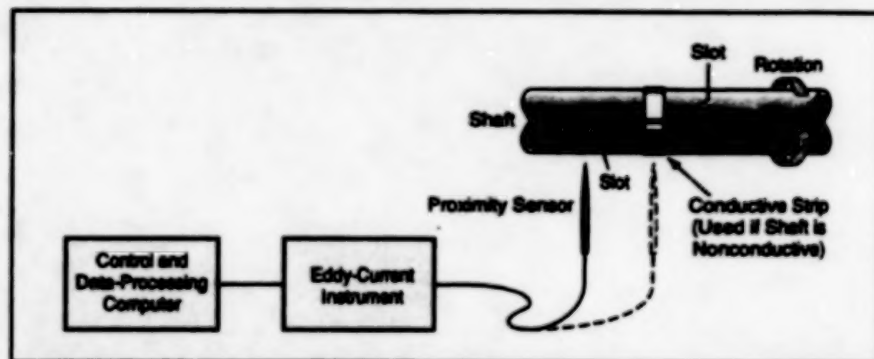
The figure illustrates a system for real-time measurement of the distance and small variations of the distance between two mechanical components that are designed to be maintained at a precise, fixed distance. In particular, the system is intended for use in measuring the lateral clearance and variations in the lateral clearance (that is, wobble) of a motor shaft relative to the motor housing while the shaft is turning. Measurement of wobble provides an early indication of wear in the motor bearings; wobble that exceeds a maximum allowable level can serve as cause for replacement of the bearings. In a systematic program for maintenance of critical machinery, it is more cost-efficient to replace bearings for cause than it is to wait for the bearings to fail or to replace bearings on a regular schedule without cause.

In this system, the lateral position of the shaft is measured by use of any of a variety of noncontact electromagnetic or capacitive proximity sensors. The sensor is mounted in a fixed position in the motor housing with its sensing tip near the lateral surface of the shaft. The surface of the shaft must be electrically conductive. If it is not conductive, then a circumferential strip of conductive or semiconductive material can be applied to the surface to provide the necessary conductivity.

Preferably, the sensor is a commercial, pencil-shaped eddy-current liftoff probe. As its name suggests, an eddy-current liftoff probe is designed to exploit the eddy-current liftoff effect, which is a variation in

the output voltage or impedance reading(s) of the probe with distance from an electrically conductive surface like that of the shaft. The tip of such a probe can have a diameter as small as 0.04 in. (1 mm), making it possible to fit the probe into a typical confined space inside a machine.

The system includes an eddy-current instrument, which contains electronic circuits that excite the probe and process the probe reading(s) into digital data. A personal computer that controls the system receives this data and processes them into distance measurements via a calibration algorithm. Measurements obtained in this way can be as accurate as 0.0004 in. (0.01 mm). The measurements can be displayed in real time in digital and/or graphical format. Optionally, the data can be processed further to analyze wobble or display indications of wobble in alternative forms or formats.



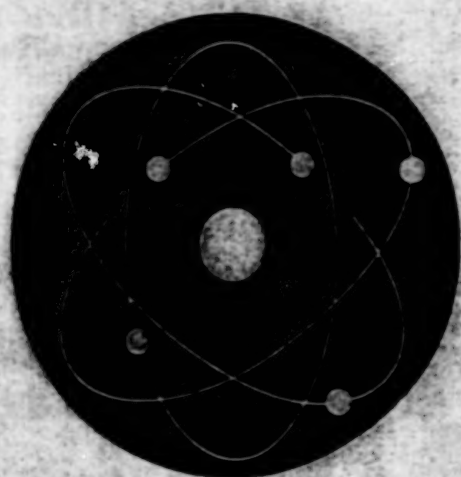
A Noncontact Proximity Sensor — preferably an eddy-current liftoff probe — provides a real-time indication of the wobble of a motor shaft in its bearings.

A slot or slots can be machined into the shaft or in the conductive or semiconductive strip on the shaft at one or more points on the circumference to provide an eddy-current discontinuity that can be used to measure the rotation of the shaft. By processing the eddy-current readings to extract and count the number of passages of the discontinuity during an observation interval, one obtains a number proportional to the speed of rotation.

This work was done by Enginn James Chen of Goddard Space Flight Center. Further information is contained in a TSP [see page 1].

This invention is owned by NASA, and a patent application has been filed. Inquiries concerning nonexclusive or exclusive license for its commercial development should be addressed to the Patent Counsel, Goddard Space Flight Center [see page 1]. Refer to GSC-13570.

BLANK PAGE



Physical Sciences

Hardware, Techniques, and Processes

- 23 Phase-Conjugate Mirror Removes Wave-Front Distortions
- 24 Fiber-Optic Differential Displacement Sensor
- 25 Liquefaction of Coal With Surfactant and Disposable Catalyst
- 25 Computing Noise Temperature in a Beam Waveguide
- 26 Water-Repellency Probe
- 27 Apparatus Tests Peeling of Bonded Rubbery Material
- 27 Mass-Flow-Meter Leak-Testing System
- 28 Oven Evaporates Isopropyl Alcohol Without Risk of Explosion
- 28 Oxygen-Mass-Flow Calibration Cell
- 29 Reducing Tilt-Related Errors of Inductive Proximity Sensors

BLANK PAGE

Phase-Conjugate Mirror Removes Wave-Front Distortions

Potential applications include multistage laser systems.

Goddard Space Flight Center,
Greenbelt, Maryland

Phase-conjugate mirrors can remove distortions or aberrations from wave fronts in laser beams. Distortions of a laser beam can be caused, for example, by thermal effects in the atmosphere, inhomogeneities in crystals, and imperfect finishes on optical surfaces. A phase-conjugate mirror is essentially a bulk index-of-refraction diffraction grating formed by the interaction between a laser beam and a nonlinear optical medium in which the beam propagates. The beam reflected back along the direction of the incident laser beam is the phase conjugate of the input beam; therefore, as it travels back through the optical media that introduced the distortions into the incident laser beam, the distortions are removed.

Phase-conjugate mirrors could be used, for example, to prevent the degradation of a laser beam that is amplified to higher power in multiple laser stages, each of which can introduce aberrations into the beam. With the help of phase-conjugate mirrors, one can obtain high-power laser beams of diffraction-limited quality. One potential application is in NASA's proposed Geoscience Laser Ranging System

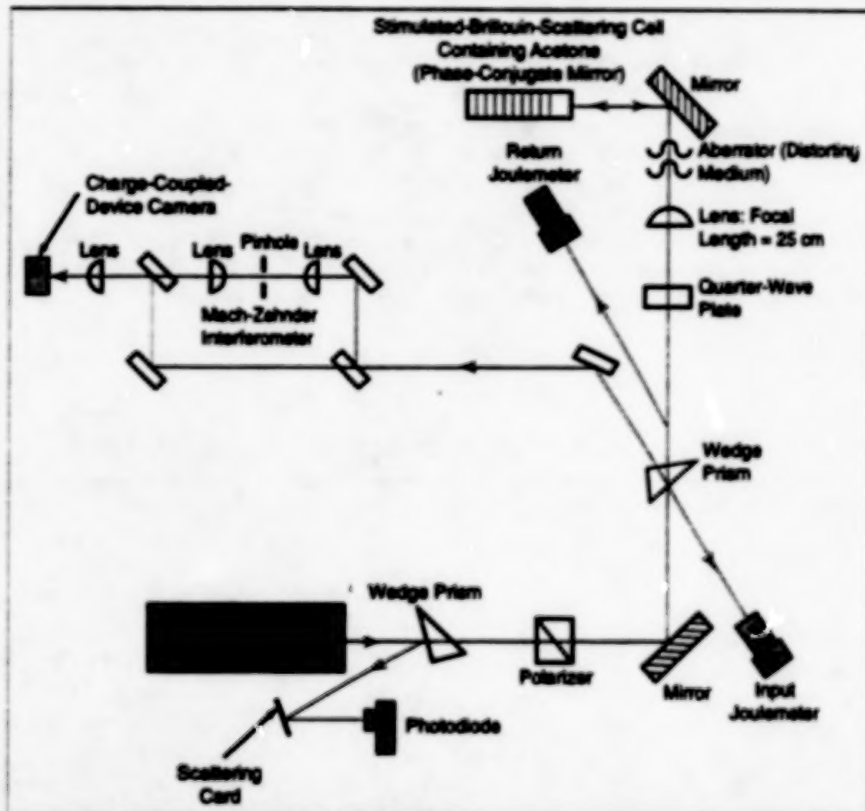


Figure 1. This Laboratory Setup can be used to demonstrate a phase-conjugate mirror.



INTERFERENCE PATTERN FORMED FROM RETURN OF UNABERATED BEAM



INTERFERENCE PATTERN FORMED FROM PHASE-CONJUGATE RETURN OF ABERATED BEAM



INTERFERENCE PATTERN FORMED FROM RETURN OF ABERATED BEAM VIA CONVENTIONAL MIRROR

Figure 2. These Interference Patterns were produced in the Mach-Zehnder interferometer of the apparatus shown in Figure 1. The effectiveness of the phase-conjugate mirror in removing most of the aberrational effects is apparent.

for an Earth-observing satellite. This instrument will include compact, efficient solid-state lasers that will be required to produce pulses of 20 to 250 mJ lasting 0.1 to 50 ns. Multistage power amplification (with its concomitant potential for introducing aberrations) will be needed to produce such pulses.

Phase-conjugate mirrors can be implemented by use of stimulated Brillouin scattering or four-wave photorefractive mixing. (Four-wave mixing can also be used in laser communications and fiber optics.)

Stimulated Brillouin scattering can occur when an intense, pulsed, laser

beam is focused into a gas or liquid. The beam interacts with the electrostrictive forces of the gas or liquid by locally heating a small volume of the material and changing its index of refraction. This interaction creates a density-and-index-of-refraction grating that travels through the material at the speed of sound. The

laser beam is Bragg-scattered off the moving grating, giving rise to a phase-conjugate backward-going (reflected) beam. The phase-conjugate/wave-front-reversal property and the associated ability to remove distortions can be used to compensate for aberrations in a double-pass amplifier by placing the phase-conjugate mirror behind the amplifier, where a conventional mirror would otherwise have been placed.

Figure 1 shows the layout of an experiment to demonstrate a stimulated Brillouin-scattering phase-conjugate mirror for a pulsed laser system. A Q-switched neodymium:yttrium aluminum garnet (Nd:YAG) laser with a 60-mJ output pulse of 20-ns duration was used as

the laser source, and acetone as the stimulated Brillouin-scattering medium. Stimulated Brillouin-scattering reflectivities as high as 60 percent were achieved. In the experiment, the cross-sectional area of a phase-conjugate beam produced by photorefractive four-wave mixing was compared with that of the return from a conventional mirror after passing back through the aberrating medium (see Figure 2). The phase-conjugate beam returned with a cross-sectional area equal to that of the unaberrated beam, but the cross section of the return from the conventional mirror was elongated.

Photorefractive four-wave mixing also gives rise to phase conjugation, but it

involves the use of a continuous-wave (instead of pulsed) laser beam and a crystal (instead of a liquid or gas). The beam is focused into the crystal (which could be barium titanate for example) and interacts with the crystal via its photorefractive properties, giving rise to a grating. As in stimulated Brillouin scattering, the beam is then reflected off the grating and becomes the phase conjugate of the input beam.

This work was done by Bernard D. Seery of Goddard Space Flight Center, Barbara J. K. Zukowski of Hughes STX Corp., and Bahak Salf of EER Systems. No further documentation is available. GSC-13554

Fiber-Optic Differential Displacement Sensor

Sensitivity to displacement is increased, while sensitivity to temperature is decreased.

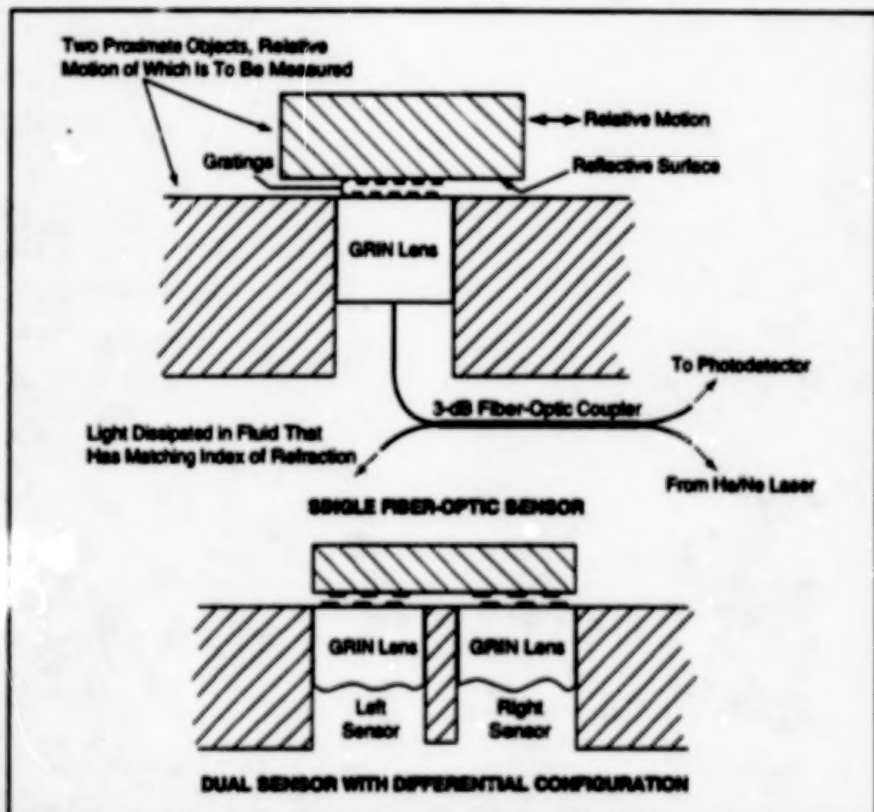
Langley Research Center,
Hampton, Virginia

The figure illustrates schematically a dual fiber-optic sensor for measuring small relative displacements of two proximate objects along a common surface. In the original application for which the dual sensor was devised, the displacement is that in a skin-friction balance on an aerodynamic surface.

The dual sensor comprises two fiber-optic sensors in a differential configuration that increases its sensitivity to displacement while decreasing its sensitivity to thermal expansion and contraction. Each component sensor includes a gradient-index-of-refraction (GRIN) lens mounted on one of the two proximate objects, an opaque/clear grating attached to the lens, and an opaque/clear grating attached to a reflective surface on the other object.

In the case of a single sensor, light supplied via a multimode optical fiber is collimated by the lens, then travels to the reflective surface, then is returned to the lens. The lens focuses the returned light into the optical fiber. The light then travels back along the fiber to a photodetector. The amount of light returned to the lens and, thus, the output of the photodetector, varies in proportion to the degree of overlap of the gratings. Therefore, a change in the output is indicative of the relative lateral displacement of the two gratings and the objects on which they are mounted.

In the case of the dual sensor, two identical gratings are attached to the reflective surface, each one facing one of the fiber-optic sensors. The two sets of grating patterns are arranged as mirror images of



In this Fiber-Optic Differential Displacement Sensor, the differential configuration doubles (in comparison with a single sensor) the sensitivity to displacement and cancels the effect of a change in temperature.

each other, so that when the two objects move relative to each other, the grating overlap in one sensor increases (with consequent increase in output) while the overlap in the other sensor decreases (with consequent decrease in output). The output of one sensor is subtracted from the

other, yielding double differential output; that is, double the sensitivity of a single sensor.

Moreover, the arrangement is such that when the two objects are in the nominal middle or neutral relative position, the overlap in both gratings is 50

percent. Thus, subtracting the outputs of the photodetectors of the two sensors at the middle position yields a null reading.

If the temperature of either proximate object changes, then thermal expansion or contraction causes the degrees of overlap

of the gratings in both sensors to increase or decrease by equal amounts. Consequently, both photodetector outputs increase or decrease by the same amount, and the net output signal obtained by subtracting them does not change.

This work was done by Ping Tcheng of Langley Research Center. No further documentation is available.
LAR-14241

Liquefaction of Coal With Surfactant and Disposable Catalyst

Fuels derived from coal may become more competitive with petroleum products.

NASA's Jet Propulsion Laboratory,
Pasadena, California

An improved coal-liquefaction process exploits the synergistic effects of a disposable iron oxide catalyst and a cheap anionic surfactant. The efficiency of conversion achieved in this process is significantly higher than the efficiencies obtained with the addition of either the surfactant or the catalyst alone. No costly pretreatment is necessary, and the increase in conversion is achieved under processing conditions milder than those used heretofore in liquefaction of coal. The quality of the distillates obtained after liquefaction in this process is expected to be superior to that of distillates obtained after liquefaction by older techniques. Further development of this process may eventually reduce the costs of fuels derived from coal enough to make such fuels competitive with petroleum products.

Fuels derived from coal have not been competitive with fuels derived from petroleum because of the high pressures and temperatures necessary to liquefy coal by older techniques, and because of the poor quality of the distillates. The state-of-the-art optimized process involves the use of supported molybdenum and nickel/molybdenum-based catalysts in two-stage ebullating reactors. The degree of conversion in this process lies in the range of 90 to 95 percent when the temperature in the reactors is 420 °C and the gauge pressure of hydrogen in the reactor is 2,200 psi (~15 MPa).

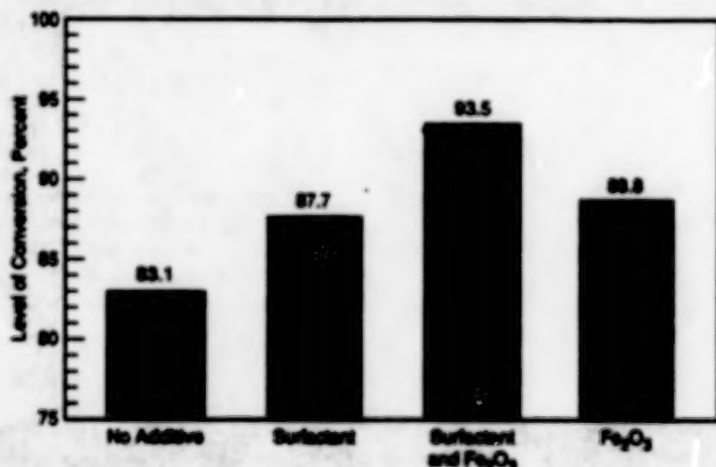
Coal fragments tend to disperse poorly in nonpolar and mildly polar solvents

and tend to agglomerate into aggregates of high molecular weight. In previous research directed toward breaking up these aggregates, the addition of surfactants was investigated. Conversion levels of about 90 percent were obtained when sodium lignosulfonate was added as a surfactant in a noncatalytic process.

In experiments that led to the improved process, specimens of coal were treated, variously, by addition of either (a) no additive, baseline case, (b) 1 percent of surfactant, (c) 1 weight percent of finely ground (particle size less than 20 µm) iron oxide powder as the catalyst, or (d) both 1 percent iron oxide and 1 percent surfactant. The process was run at a temperature of 375 °C, with hydrogen at a

gauge pressure of 1,800 psi (~12 MPa) for 1 hour. The levels of conversion achieved in cases (a), (b), (c), and (d) were 83.1, 87.7, 88.8, and 93.5 percent, respectively (see figure). This result indicates that addition of the iron oxide and surfactant can exert a positive synergistic effect on the liquefaction of coal. It has been conjectured that the surfactant improves the hydrodynamics in the reactor, enabling the coal to come into more intimate contact with the catalyst.

This work was done by Gregory S. Hickey and Premal K. Sharma of Caltech for NASA's Jet Propulsion Laboratory. Further information is contained in a TSP [see page 1].
NPO-19221



The Level of Conversion achieved by addition of both the surfactant and the catalyst is greater than that achieved by addition of either alone.

Computing Noise Temperature in a Beam Waveguide

Contributions from spillover are treated semiempirically.

A method of computing the noise temperature in a beam waveguide system (see figure) involves both theoretical and experimental elements. The method circumvents the problem of computing

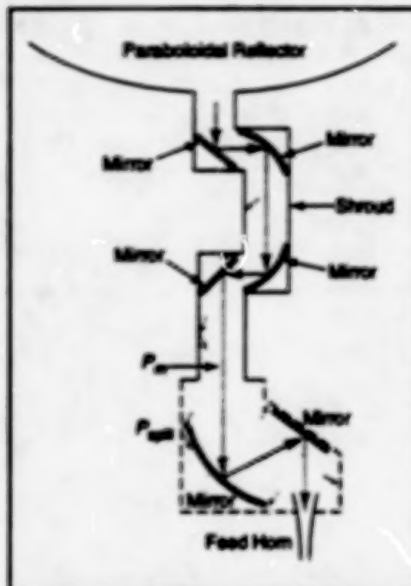
the noise temperature exactly from first principles: in the case of a typical practical system, the noise-temperature problem is so complex and difficult that an exact solution is impossible.

NASA's Jet Propulsion Laboratory,
Pasadena, California

In this method, the noise temperature, T_{BWG} , is expressed as a sum of two parts: $T_{\text{BWG}} = T_m + T_{\text{sp}}$. Similarly, the total beam power, P_{BWG} , is expressed as $P_{\text{BWG}} = P_m + P_{\text{sp}}$. P_m is that part of the

beam power that is always confined inside all mirrors. P_{sp} is the sum of each mirror that is mainly dissipated and converted to noise by multiple reflections and absorption in the shroud and behind the mirrors. T_m and T_{sp} are the contributions to T_{BWG} associated with P_m and P_{sp} respectively. T_m is given by $T_m = \alpha_m \beta$, where $\alpha_m = P_m/P_{BWG}$ and β is a function of the frequency of the beam and the temperature and electrical resistivity of the mirrors. The value of α_m and β can be computed accurately. However, because of the complexity of the multiple reflections and absorptions T_{sp} cannot be computed analytically. The technique used to compute T_{sp} will be described next. The noise temperature T_{sp} is given in a form $T_{sp} = \alpha_{sp} T_0$ where $\alpha_{sp} = P_{sp}/P_{BWG}$ and T_0 is an effective noise temperature (in Kelvin) seen by P_{sp} and determined empirically.

Combining results from the foregoing equations, the total noise temperature can be expressed as $T_{BWG} = \alpha_m \beta + \alpha_{sp} T_0$. If at least one measurement of



A Beam Waveguide System associated with a large paraboloidal antenna includes mirrors enclosed in a shroud. Contributions to noise are associated with the transmitted power, P_m , and the spillover power, P_{sp} .

T_{BWG} in a beam waveguide of representative design is available, it can be used to compute $T_0 = (T_{BWG} - \alpha_m \beta) / \alpha_{sp}$. Thereafter, it is not necessary to repeat measurements of T_{BWG} . Instead, one can use the computed value of T_0 under the assumption that it is applicable to any beam waveguide of similar design, including a shroud structure with nearly the same electrical resistivity and frequency.

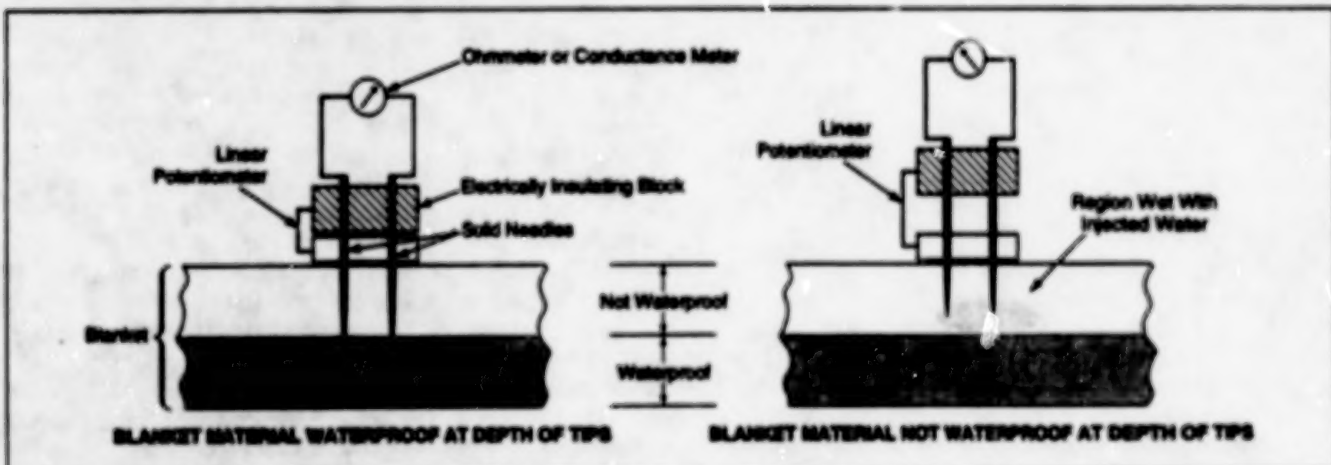
In the case of a long and/or complicated beam waveguide, more accurate results can be obtained by dividing α_{sp} into α_1 and α_2 and the corresponding noise-temperature coefficients into T_1 and T_2 . Then $T_{sp} = \alpha_1 T_1 + \alpha_2 T_2$, the 1 and 2 components representing contributions from different parts of the waveguide structure.

This work was done by Watt Veruttipong and Manuel M. Franco of Caltech for NASA's Jet Propulsion Laboratory. Further information is contained in a TSP [see page 1]. NPO-19119

Water-Repellency Probe

A simple measurement reveals the presence or absence of waterproofing material in a blanket.

Lyndon B. Johnson Space Center,
Houston, Texas



Nonwaterproof Blanket Material Wicks Injected Water, allowing the path between the tips of the needles to become electrically conductive. Waterproof blanket material does not wick injected water, preventing the formation of an electrically conductive path between the tips.

An instrument yielding the presence or absence of waterproofing agent at any given depth in a blanket has been developed. In its original application, the blankets in question were part of the space shuttle thermal protection system. The instrument was utilized to determine the extent of waterproofing "burnout" due to re-entry heating and adverse environment exposure. Areas which do not have substantial waterproofing removal become

candidates for elimination of this process in the following flow.

The instrument (see figure) includes two needles which are electrically insulated except for the very tip. The needles are connected to an ohmmeter to measure electrical conductance between the two probes. A small amount of deionized water is applied to the surface of the blanket. The water creates an electrically conductive media in the nonwaterproofed

region of the blanket. The needles are slowly removed from the surface of the blanket at a consistent rate. When the needles penetrate the boundary between the nonwaterproofed and waterproofed regions, the electrical conductivity between the probes decreases. When the conductivity decreases below a predetermined setpoint, an alarm indicates the waterproofed region has been reached. A linear potentiometer provides a digital

readout of the waterproofing burnout depth. The measurement is repeated at several points in each blister from which an average burnout depth is obtained.

This work was done by Charles D. Rosen, Shirley M. Mitchell, Stanley R. Jolly, Richard G. Jackson, Scott T. Fleming, William J. Roberts, and Daniel R. Bell of

Rockwell International Corp. for Johnson Space Center. Further information is contained in a TSP [see page 1], MSC-22295

Apparatus Tests Peeling of Bonded Rubbery Material

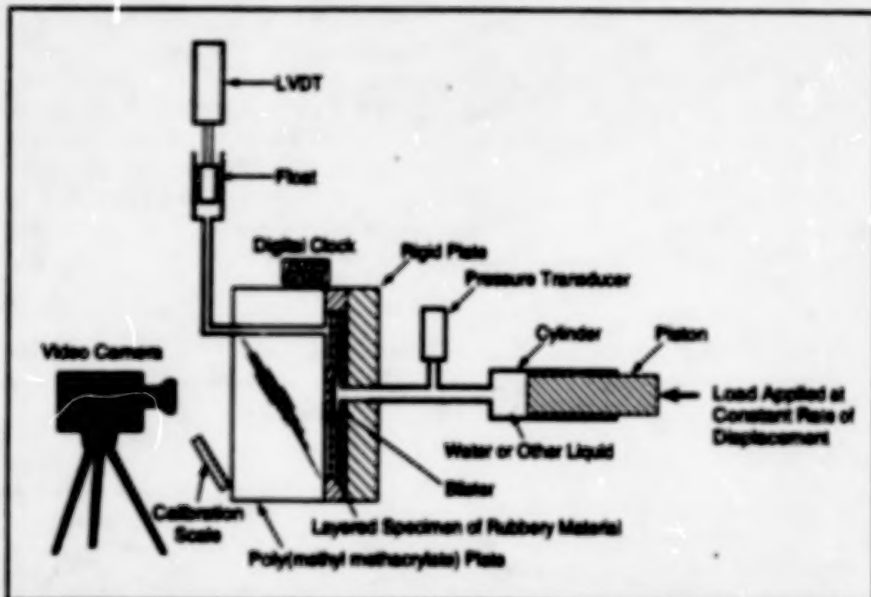
Growth of a blister under pressure is measured.

Marshall Space Flight Center, Alabama

The figure illustrates an instrumented hydraulic constrained blister-peel apparatus used to obtain data on the degree of bonding between a specimen of rubbery material and a rigid plate. (In the original application, the rigid plate is made of steel, and the specimen of rubbery material is a rectangular layered slab of solid rocket propellant, liner, and insulator material bonded to the plate with an adhesive material.) The data from blister-peel tests can be used to determine critical fracture-energy release rates of such bonds.

In preparing the specimen and the rigid plate, a thin polytetrafluoroethylene disk is placed at the center to form a central circular unbond from which the blister can grow. A liquid (typically, water) pressurized by a piston is admitted to the blister through a central hole in the rigid plate. Growth of the blister is constrained by a thick polymethyl methacrylate plate, which is transparent. A video camera observes the growth of the blister through the transparent plate.

Pressure in the water or other liquid is measured by a pressure transducer. The volume of liquid pumped into the blister is measured and controlled via displacement of the piston. The volumetric rate can also be measured and controlled; this is important because the blister-peel behavior of a specimen can be highly



Growth of a blister is tracked by a video camera, digital clock, pressure transducer, and a piston-displacement sensor. Cylinder pressure is controlled by a hydraulic actuator system. The linear variable-differential transformer (LVDT) and float provide a second, independent measure of change in blister volume that can be used as more precise volume feedback in a low-growth-rate test.

dependent on the rate of growth.

Time, pressure, and volume data are recorded digitally during the test. The size of the blister is computed from the digitized video image of the blister captured by a video frame grabber. From the foregoing data, a computer calculates the

total energy released in each increment of growth of the blister.

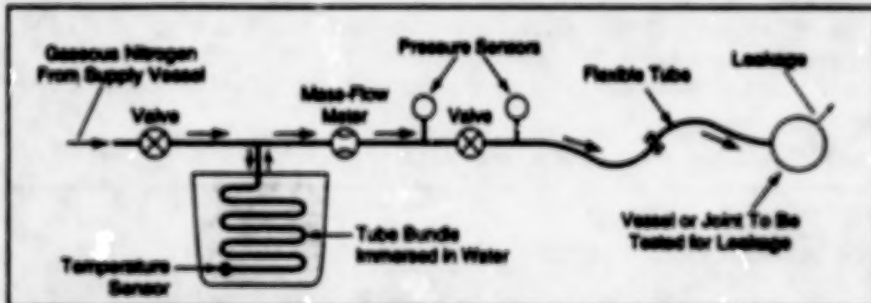
This work was done by Russell A. Crook and Robert Graham of Thermo Corp. for Marshall Space Flight Center. Further information is contained in a TSP [see page 1], MFS-28878

Mass-Flow-Meter Leak-Testing System

This system provides more data, more accurately, in less time than did its predecessor.

Marshall Space Flight Center, Alabama

An improved leak-testing system incorporates a mass-flow meter as the primary sensor for measurement of the leakage rate. The system was developed to replace a leak-testing system based on measurement of pressure-decay rate after initial pressurization of a joint or vessel to be tested. In comparison with its predecessor, the improved system is easier to use and more reliable and it enables leak tests to be completed in 30 to 40 percent less time. In addition, it produces test data that are more plentiful.



Nitrogen is supplied at regulated pressure to a sealed joint or vessel to be tested for leakage. Rate of flow indicated by the mass-flow meter serves as a measure of the size of the leak.

ful, more accurate, and better suited to leak detection and diagnosis.

In the improved system, nitrogen (the testing gas) is supplied at regulated pressure to the vessel or joint to be tested, and the rate of flow of nitrogen through the vessel or joint is measured to obtain an indication of the size of the leak. The nitrogen is fed to the mass-flow meter and the test article via a tube bundle that is immersed in a tank of water for thermal stability (see figure). The tube bundle is standard tubing wrapped in a compact shape which acts as a reservoir, thereby facilitating regulation of the pressure.

The mass-flow meter contains a heated sensor tube through which the nitrogen flows. Temperature sensors in the

heated tube produce readings indicative of the rate at which the flowing nitrogen carries away heat from the tube. The rate of flow is related to the heat-transfer rate in a known way and is thus computed from these readings.

The leak-testing system is controlled by a computer in which expert-system software monitors sensor data in real time and alerts personnel to out-of-tolerance test conditions. Software controls pretest and posttest verification of integrity of the instrumentation, controls the test procedures, and monitors the configuration of hardware and the test parameters.

The system operates over a range of test conditions, including pressures from atmospheric to 1,000 psi (0.1 to 6.9 MPa), temperatures from 50 to 120 °F (10 to

49 °C), and volumes from < 1 in.³ to 22 in.³ (<16 cm³ to 361 cm³). The system is even sensitive enough to measure absorbed gas seeping from O-ring seals after test pressure has been released.

This work was done by Eric B. Sorensen of Marshall Space Flight Center; Andre V. Polidori, Joe R. Heman, and Holland L. Dresser of Thiokol Corp.; and John Hellum of Cooper Oil Tool. Further information is contained in a TSP [see page 1].

Inquiries concerning rights for the commercial use of this invention should be addressed to the Patent Counsel, Marshall Space Flight Center [see page 1]. Refer to MFS-31002.

Oven Evaporates Isopropyl Alcohol Without Risk of Explosion

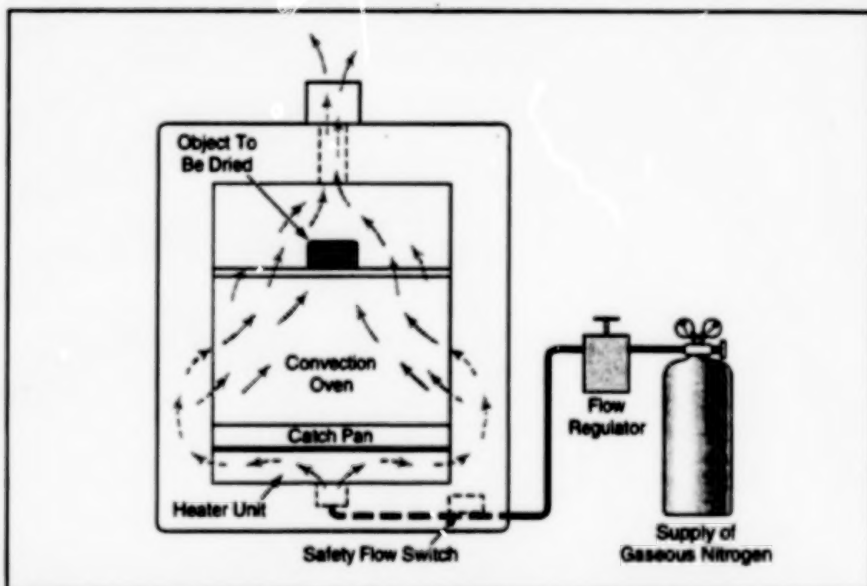
A convection oven can be made explosion-proof at relatively low cost.

Marshall Space Flight Center,
Alabama

An ordinary convection oven with a capacity of 1 ft³ (0.028 m³) has been modified for use in drying objects that have been washed in isopropyl alcohol. The oven can probably also be used to evaporate other flammable solvents. The oven costs \$375; the materials used in modifying it to make it explosion-proof for evaporating isopropyl alcohol cost less than \$200. In contrast, a typical commercial explosion-proof oven costs at least \$10,000 (1993 prices).

The modifications were (see figure) the installation of equipment to purge the interior of the oven with gaseous nitrogen, the addition of a catch pan over the heater unit, and the installation of a safety flow switch and a door interlock. The safety flow switch keeps the oven turned off unless the nitrogen is flowing.

An object to be dried is placed on the top shelf of the oven and the door is closed. The flow of nitrogen is turned on, then the oven is turned on. The temperature in the oven is monitored and is not allowed to exceed 250 °F (121 °C). Typically, the object is kept in the oven at the max-



Nitrogen-Purge Equipment and safety interlocks are added to a convection oven to prevent explosive ignition of flammable solvent evaporating from the object to be dried.

imum temperature for at least 90 min. The oven is allowed to cool to 100 °F (38 °C) before the door is opened.

This work was done by Gene E. Morgan and William S. Huft of Rockwell

International Corp. for Marshall Space Flight Center. Further information is contained in a TSP [see page 1]. MFS-30050

Oxygen-Mass-Flow Calibration Cell

The flow of oxygen ions in a solid electrolyte would be proportional to the applied electric current.

NASA's Jet Propulsion Laboratory,
Pasadena, California

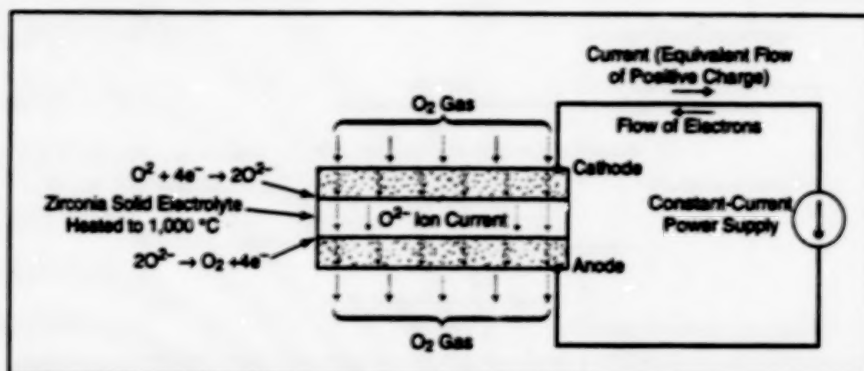
A proposed calibration standard for the mass flow rate of oxygen would be based on the conduction of oxygen ions through a solid electrolyte membrane

made of zirconia and heated to a temperature of 1,000 °C. An electric current applied through such a membrane in the presence of oxygen causes oxygen to

be transported through the membrane at a rate proportional to the current, the proportionality being one oxygen molecule (O₂) for every four electrons. An oxy-

gen-mass-flow calibration cell based on this concept could be used to calibrate a variety of medical and scientific instruments that are required to operate with precise rates of flow of oxygen.

Older mass-flow-rate calibration standards are based, variously, on measurements of temperatures, pressures, and volumes, all of which affect each other. Errors in these measurements tend to be cumulative and to affect the final calibration mass flow rates. In contrast, the proposed standard would be unaffected by variations in temperature and pressure, and would not require measurement of volume; electric current is the only parameter that would affect the rate of flow. Thus, by maintaining a constant, precise direct current, one could maintain a precise mass flow rate of oxygen; in principle, the flow could be



Oxygen ions would be transported through heated zirconia by the applied electric current. One oxygen molecule would be pumped through the zirconia membrane for every four electrons pushed around the circuit by the power supply.

maintained at the desired rate with an error much smaller than 1 percent.

This work was done by Robert E. Martin of Caltech for NASA's Jet Propulsion

Laboratory. Further information is contained in a TSP [see page 1].
NPO-19327

Reducing Tilt-Related Errors of Inductive Proximity Sensors

Hemispheres centered in the sensing coils enable more accurate placement of the sensors.

Marshall Space Flight Center,
Alabama

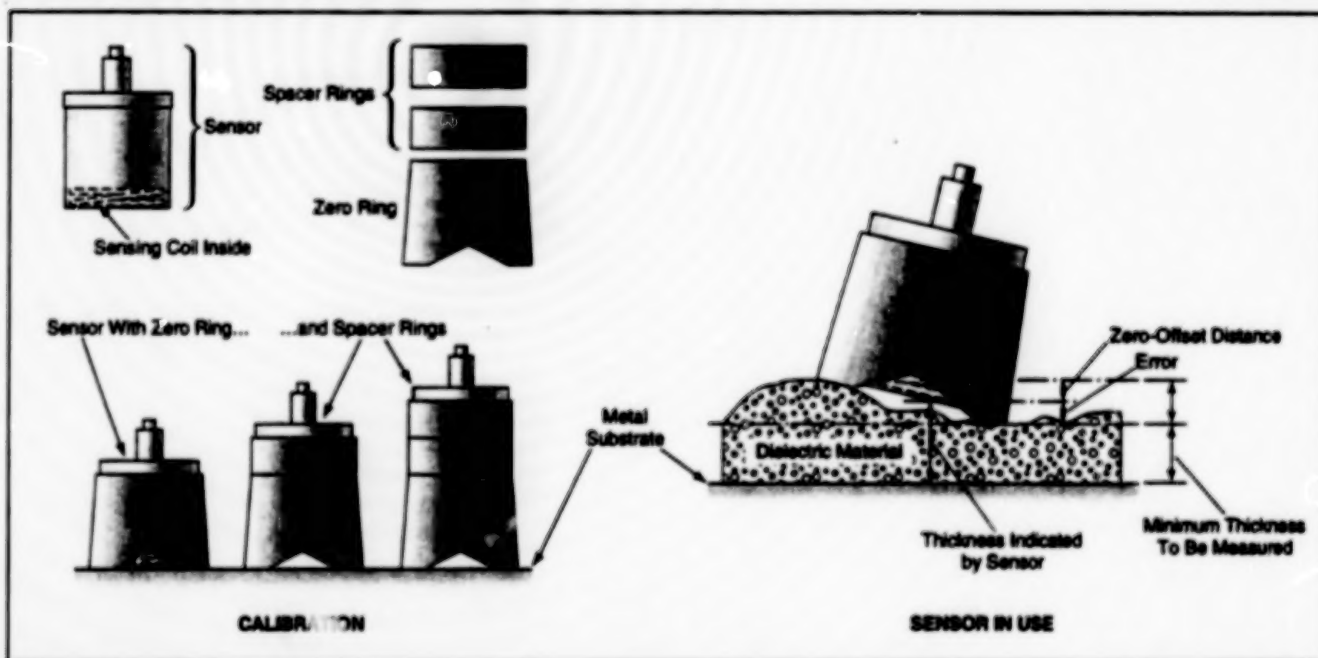


Figure 1. The Thickness Indicated by the Sensor differs from the minimum thickness that one seeks to read when the surface of the dielectric layer is uneven.

A simple modification of an inductive proximity sensor nearly eliminates the tilt-related readout error that occurs when the sensor is used to measure the thickness of a dielectric layer on a metal substrate (e.g., to measure the thickness of an insulating blanket on a boiler). This modification can take any of several forms, all of which are equivalent to the addition of a hemispherical contact surface, as explained in more detail below.

As shown in the left part of Figure 1, an inductive proximity sensor is calibrated to read zero distance from the metal substrate when the sensing coil lies at a nominal small distance, called the "zero-offset distance," from a flat metal substrate. The sensor is also calibrated at a number of other known distances. During the zero calibration and in use, the sensing coil is fitted with a dielectric "zero ring" — a shoe that, when placed in contact with the sub-

strate, keeps the probe at the zero-offset distance.

At small tilt angles, the sensor reading is nearly independent of the tilt per se. However, the reading depends on the perpendicular distance from the center of the probe coil to the surface of the metal substrate, and this distance can depend on the tilt under some circumstances. For example, the right part of Figure 1 shows how a tilt-related error can occur when

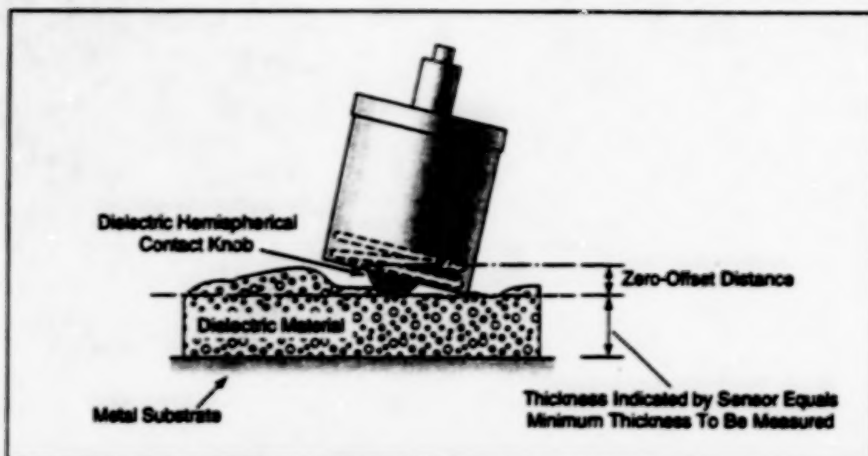


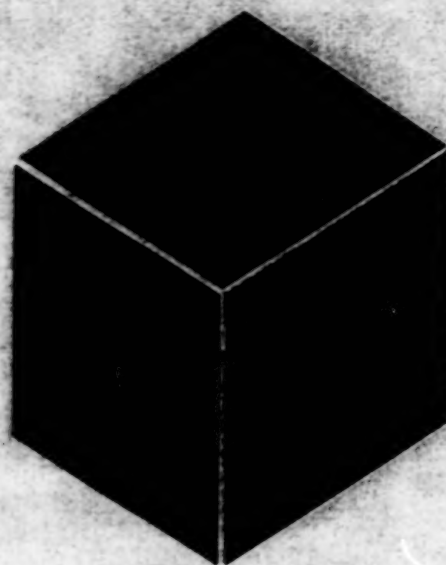
Figure 2. The Sensor Indicates the True Thickness when equipped with a hemispherical contact knob that ensures the correct zero-offset distance at the measurement location.

the sensor is used to measure the minimum thickness of an uneven dielectric layer. Because of the unevenness in the thickness and the resulting tilt, the perpendicular distance is altered such that

the zero-offset location of the probe corresponds to a thickness greater than the minimum thickness that one seeks to measure. As a result, the thickness reading of the sensor is too high.

Figure 2 shows a sensor modified to reduce the tilt-related error. The zero ring is removed; in its place, a dielectric contact knob with a hemispherical surface is attached. The hemispherical surface is centered at the center of the coil and has a radius equal to the zero-offset distance. The contact knob can be placed in contact at the desired measurement location on the dielectric layer to be measured, ensuring that the center of the coil lies at the correct zero-offset perpendicular distance from the desired measurement point. Thus, the perpendicular distance indicated by the probe readout equals the thickness that one seeks to measure.

This work was done by Glenn M. Cotty, Jr., of Lockheed Martin for Marshall Space Flight Center. Further information is contained in a TSP [see page 1].
MFS-31092



Materials

Hardware, Techniques, and Processes

- 33 Polyimides That Contain Pendent Siloxane Groups
- 34 Cleaning Spectralon™ To Maintain Reflectance Properties

BLANK PAGE

Polyimides That Contain Pendent Siloxane Groups

The pendent siloxane groups impart properties that are desirable in some applications.

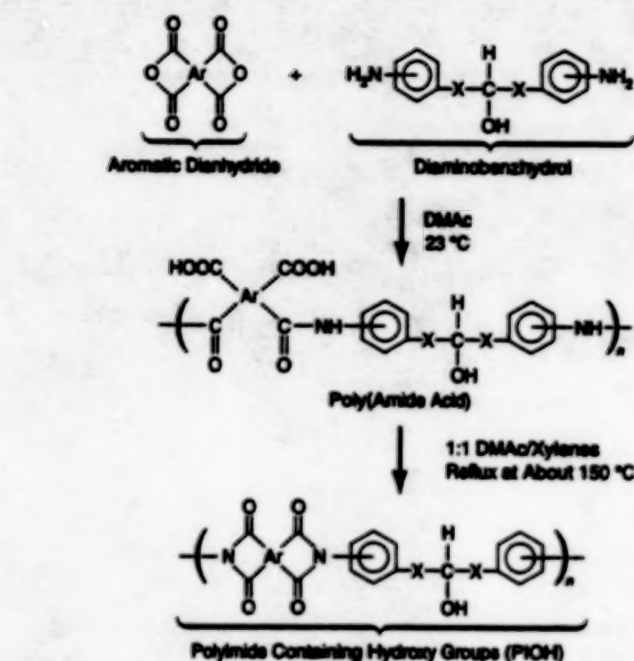
Langley Research Center,
Hampton, Virginia

Polyimides that contain pendent siloxane groups (PISOXs) can be synthesized from polyimides that contain hydroxy groups (PIOHs) according to either of two alternative approaches. The addition of pendent siloxane groups to a polyimide decreases its dielectric constant, and decreases its absorption of moisture; these changes in properties are advantageous in some electronic applications. The pendent siloxane groups on polyimides also enhance resistance to atomic oxygen in that they undergo slight degradation to form a protective silicon oxide coats when exposed to atomic oxygen.

Experiments that demonstrated both alternative approaches to the synthesis of PISOXs began with the synthesis of the precursor PIOHs. Each synthesis of a PIOH (see Figure 1) began with the reaction of an aromatic dianhydride with a diaminobenzohydrol compound in dimethyl acetamide (DMAc) at a temperature of 23 °C to obtain a poly(amide acid). The poly(amide acid) was then added to a solution of DMAc and xylenes refluxing at a temperature of 150 °C to effect thermal cyclization of the poly(amide acid) to the PIOH. A PIOH prepared in this way remains soluble, whereas a poly(amide acid) that is cast into a thin film and then thermally cyclized cannot be redissolved in DMAc or other suitable solvents (the PIOH must remain soluble in order to use it to synthesize a PISOX).

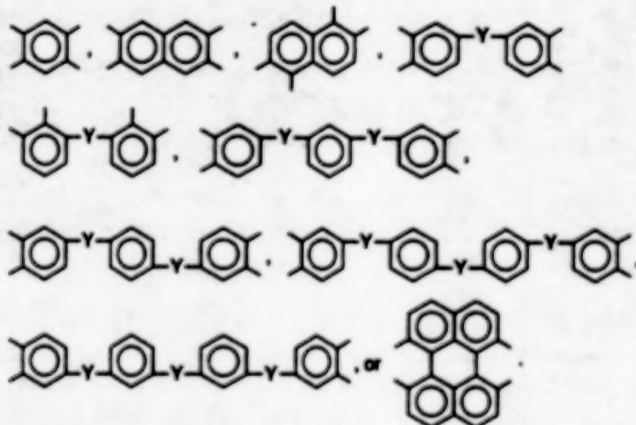
Figure 2 illustrates the two alternative approaches to the synthesis of a PISOX from a PIOH. In one approach, a hydrogen-terminated siloxane compound or oligomer dissolved in toluene was added to a DMAc solution of the PIOH containing a catalytic amount of chloroplatinic acid ($H_2PtCl_6 \cdot 6H_2O$). The reaction mixture was stirred at room temperature for about 16 h under nitrogen. The solution was subsequently cast and dried to obtain the polymer product in the form of a thin solid film. The other approach was similar except that chloroplatinic acid was not used; a chloro-terminated silicon compound or oligomer was used instead of the hydrogen-terminated siloxane compound or oligomer, and hydrochloric acid was evolved during the reaction.

The PISOX films thus formed were translucent, with colors varying from tan

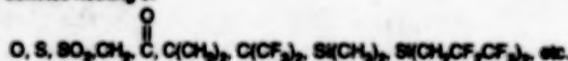


Notes:

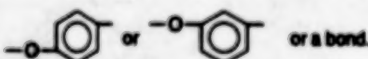
1. Ar denotes



2. Y denotes nothing or



3. X denotes



3. n denotes an integer between 1 and 1,000.

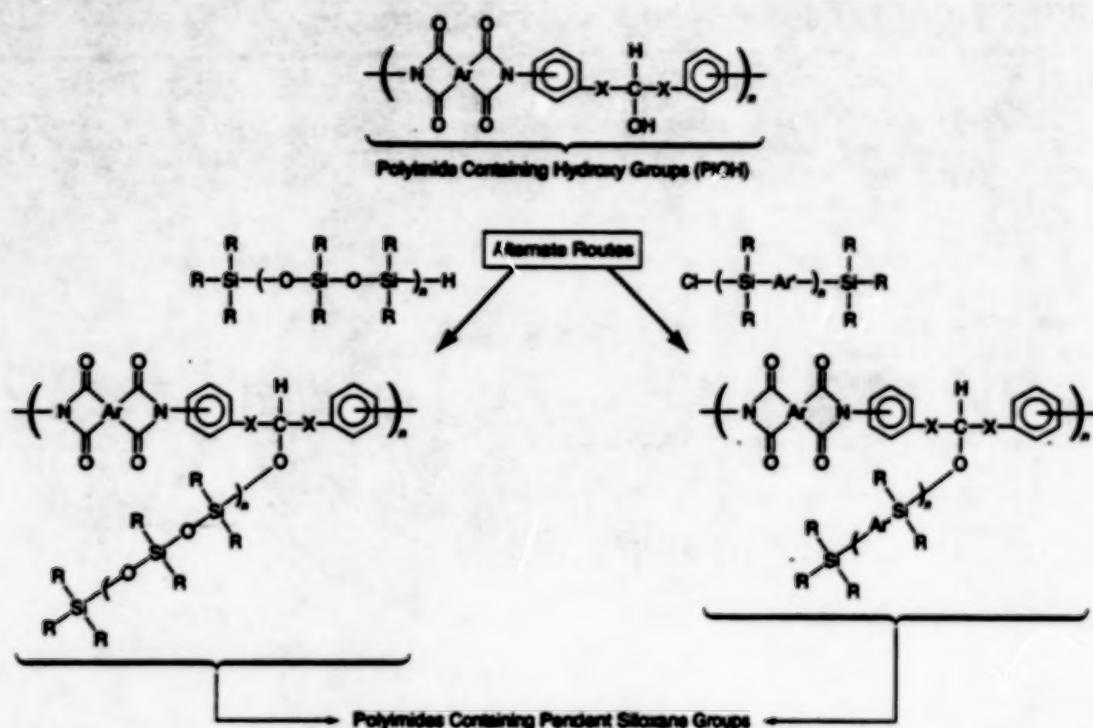
Figure 1. Polyimides Containing Hydroxy Groups (PIOH) are synthesized as soluble precursors to polyimides that will contain pendent siloxane groups.

to light brown. The glass-transition temperatures of the PISOXs ranged from 167 to 235 °C. Thermogravimetric analysis showed 5-percent losses of weight at temperatures near 380 °C in both air and nitrogen. The tensile strengths and tensile moduli of the films were in the range of 8.2 to 15.6 kpsi (57 to 108 MPa) and 248 to

453 kpsi (1.71 to 3.12 GPa), respectively.

This work was done by John W. Connell, Terry L. St. Clair, and Paul M. Hergenrother of Langley Research Center. Further information is contained in a TSP [see page 1].

This invention has been patented by NASA (U.S. Patent No. 5,304,627).



Notes:

1. R denotes

CH_3 , CH_2CH_3 , $(\text{CH}_2)_2\text{CH}_3$, $\text{CH}(\text{CH}_3)_2$, C_6H_5 , $(\text{CH}_2)_2\text{CF}_3$, etc.

2. Ar' denotes , CH_2 , CH_2CH_2 , OCH_2O , CF_2 , CF_2CF_2 , OCF_2O , etc.

3. X and n are as defined in Figure 1.

Figure 2. Pendent Siloxane Groups of two different types are incorporated according to two alternative approaches.

Inquiries concerning nonexclusive or exclusive license for its commercial

development should be addressed to the Patent Counsel, Langley Research

Center [see page 1]. Refer to LAR-14638.

Cleaning Spectralon™ To Maintain Reflectance Properties

Vacuum baking removes impurities that participate in photochemical degradation under ultraviolet light.

Spectralon™ is a unique and potentially important reflectance material for space applications due to its highly Lambertian reflectance distribution function, which is maintained over a long wavelength range. As supplied by the manufacturer, Spectralon™ is quite stable and retains its reflectance properties indefinitely in most terrestrial and extraterrestrial environments.

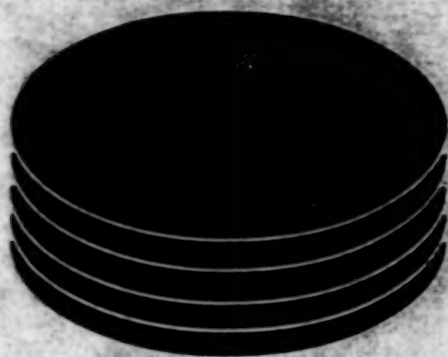
For specialized applications, however, in which the material is exposed to ultraviolet or vacuum-ultraviolet radiation, degradation in its reflectance properties, particularly in the low wavelength region of the spectrum, is observed. These changes are due to trace amounts of volatile hydrocarbon impurities, inherent in the resin used to manufacture Spectralon™ that, upon irradiation, convert into a yellow

absorbing layer on the surface. These hydrocarbon impurities can be removed and the stability of Spectralon™ towards ultraviolet and vacuum-ultraviolet radiation greatly enhanced by baking the material at 90 °C for 24 h in a vacuum of 10^{-6} torr (about 10^{-4} Pa). After the vacuum bake, the material should be handled with white, cotton, lint-free gloves in a clean environment (preferably a clean room). As the material has a tendency to reabsorb volatile organic compounds, it should be stored and transported only in clean, airtight (preferably glass or oil-free metal) containers. The material should not be placed in plastic containers or bags because plasticizers and organic antistatic agents can readily leach from those containers and recontaminate the materials.

NASA's Jet Propulsion Laboratory,
Pasadena, California

Spectralon™, cleaned and handled in the described manner, is photochemically stable and maintains its reflectance properties, even after extensive exposure to solar ultraviolet light. It should be noted that, except for these trace volatile hydrocarbons, Spectralon™ is a very pure material, and cleaning procedures which utilize washing, particularly with organic solvents, can frequently increase the contamination level and should be avoided.

This work was done by Albert Stigman, Carol Bruegge, and Gary Plett of Caltech for NASA's Jet Propulsion Laboratory. Further information is contained in a TSP [see page 1].
NPO-19048



Computer Programs

Electronic Systems

- 37 Program Computes Receiver Gain and Noise Profiles

Fabrication Technology

- 37 Program Simulates a Modular Manufacturing System

Mathematics and Information Sciences

- 37 Quantifying Danger to Spacecraft Crews From Orbital Debris
38 Windowing System for Test and Simulation

BLANK PAGE

Computer Programs

These programs may be obtained from COSMIC. Please contact

COSMIC®

Computer Services Annex
University of Georgia
Athens, GA 30602
Telephone No. (404) 542-3265.

Electronic Systems

Program Computes Receiver Gain and Noise Profiles

Performance figures are presented on a spreadsheet.

RCVRPROF computer program is a computer-aided-design (CAD) software tool useful in the analysis and design of communication receivers and downconverters. RCVRPROF provides a customized spreadsheet with formulas and graphs that provide a detailed description of performance of a receiver. Such performance parameters as noise temperature, gain, noise power, noise spectral density, and dynamic range are analyzed for the contribution of each to overall performance of the receiver.

The spreadsheet is constructed by listing each component of the receiver in order, beginning with the antenna. Each component is described as either "amp" or "pad." If the component has independent gain and noise temperature, then it is of "amp" type (gain in dB can be positive or negative). If the component is passive and its noise temperature and gain are related, it is of the "pad" type, and the only parameter that one need enter is its gain (negative in dB).

The RCVRPROF spreadsheet contains input and output columns, as well as two charts that graphically represent the data. The input parameters are component name, noise temperature, gain, output 1-dB compression point, bandwidth, and signal level. The output parameters are system noise temperature, total system gain, noise power spectral density, total noise power in the band, dynamic range, and headroom. Graphically, one chart shows the contribution of each component to the receiver system noise temperature, while the other shows a gain profile of the receiver chain with the signal level

compared to the 1-dB compression point and the receiver noise floor. The charts can be tailored for the specific application.

RCVRPROF has been implemented as a spreadsheet program by use of Lotus 1-2-3 v1.0 and Microsoft Excel v4.0, both for Microsoft Windows v3.1. The standard distribution medium for RCVRPROF is a 3.5-in. (8.89-cm), 1.44MB, MS-DOS-format diskette. Documentation is included in the price of the program. RCVRPROF was released in 1994 and is a copyrighted work with all copyright vested in NASA.

This program was written by Dale McWatters of Caltech for NASA's Jet Propulsion Laboratory. Further information is contained in a TSP [see page 1].
NPO-19472

Fabrication Technology

Program Simulates a Modular Manufacturing System

All machine operators are assumed to be equally trained and capable.

SSE is a computer program that provides a simulation environment for modeling manufacturing systems that contain relatively small numbers of stations and operators. As a result, the simulation model need not be complex, with the exception of those parts that represent movements of machine operators. SSE has been designed to simulate manufacturing of apparel, but can also be used in other manufacturing domains. SSE is an excellent simulation software package for small or medium-size firms including those that lack the expertise to develop detailed models or have only minimal knowledge in describing manufacturing systems and in analyzing the results of simulations on mathematical models. The user does not need to know a simulation language to use SSE. SSE has been used by a number of apparel-manufacturing firms to design new modules and to evaluate existing modules.

SSE can be used to design and evaluate a modular manufacturing system with one line and a maximum of 18 sta-

tions in a series. Each station can include a maximum of eight machines performing identical operations in parallel. A maximum of 26 operators is allowed, and all are assumed to be cross-trained and to be able to work at any station at the same efficiency. SSE can include unlimited space for work in process in front of each station. There must always be enough items in front of the first station to prevent a delay while waiting for an item. Work is done in lots; a lot can consist of one or many items. SSE also incorporates the assumption that there are no machine breakdowns.

This program was originally written in Turbo C v2.0 for IBM PC-compatible computers running MS-DOS and has been successfully implemented by use of Turbo C++ v3.0. Sample MS-DOS executable codes and sample input/output files are included on the distribution medium. The program requires a VGA graphics display and at least 128K of random-access memory for execution. The standard distribution medium for this program is one 5.25-in. (13.335-cm), 360K, MS-DOS-format diskette. This program was developed in 1992.

This program was written by Bernard J. Schroer and Jian Wang of the University of Alabama in Huntsville for Marshall Space Flight Center. Further information is contained in a TSP [see page 1].
MFS-26245

Mathematics and Information Sciences

Quantifying Danger to Spacecraft Crews From Orbital Debris

Probabilities of crew injury or loss are estimated by Monte Carlo-style simulations.

The MSCSurv computer program is designed to quantify the conditional probability of losing one or more crew members following the remote likelihood of penetration of orbital debris into a cluster of spacecraft modules that contain crew members. Contributions to the probability of losing

one or more crew members are quantified from three significant penetration-induced hazards: rupture of a pressure wall (explosive decompression), injuries induced by fragments, and "slow" depressurization. MSCSurv uses a Monte Carlo-style sub-routine to simulate the penetration of thousands of orbital debris particles of various sizes, velocities, and angles of approach (selected according to their NASA-based environment distribution) into a spacecraft of selected exterior geometry. The file of data that specifies this exterior geometry can be created and/or altered by use of a simple spreadsheet program.

Other MSCSurv input files include crew position as a function of time and interior constructions (i.e., protective capabilities) of the spacecraft. In addition to the input files, MSCSurv is programmed to query the user on a variety of assumptions that can alter the probability of losing one or more crew members (crew sleep position, hole-size model, critical crack length prior to rupture of a pressure wall, and the like).

Outputs from the program include (1) values of the probability of losing one or more crew members, both for the entire spacecraft and for each individual module and (2) locations of crew injuries and losses throughout the spacecraft. Through alteration of input assumptions, the user can identify which alterations of the design of the interior of the spacecraft and which alterations of crew protocols can quantifiably improve overall spacecraft safety for occupants following penetration by orbital debris.

MSCSurv was written in FORTRAN 77 for IBM PC-series and compatible computers running MS-DOS. It has been successfully implemented on a DECpc 486-series computer running MS-DOS 6.2. The Microsoft FORTRAN compiler v4.0 or higher is necessary for recompilation of the source

code. The standard distribution medium for MSCSurv is a 3.5-in. (8.89-cm), 1.44MB, MS-DOS-format diskette. MSCSurv was released in 1994 and is a copyrighted work with all copyright vested in NASA.

This program was written by Joel Williamsen of Marshall Space Flight Center. Further information is contained in a TSP [see page 1].
MFS-31022

Windowing System for Test and Simulation

The application programmer's interface is simple, small, and powerful.

The Windowing System for Test and Simulation (WFI) computer program is a Turbo-Pascal-class library that enables the easy and flexible writing of data to window-type displays. Many windowing systems require large amounts of memory and processing time for bit-mapped graphics, and include complicated application-programming interfaces. By using character-based graphics, WFI lessens the load on both the central processing unit and on the bus. The application programmer's interface in WFI is simple, small, and powerful, eliminating the steep learning curve of other window programming systems. Each routine has been specifically designed to operate in real-time testing and measurement environments or as a part of a simulation process.

This package of software is intended to be embedded in the user's own software for development of application programs. In many cases, functionality may be extended or modified, without changing the source code as it is written, by use of

object-oriented programming techniques.

Three window object types are derived from the base-class *BOEWindow*: *VDI*, *VST*, and *HelpWindow*. The *VDI* (Virtual Dumb Terminal) object contains methods for simple text display, automatic logging, and scrolling. The *VST* (Virtual Smart Terminal) object provides a functional equivalent of the Turbo Pascal screen, with a simple user interface, cursor addressing, a variety of text colors and attributes, and logging. The *HelpWindow* is used for viewing text files, which are typically help files or source code.

These three window types, when created, are placed on a heterogeneous list called "Wall." The Wall object points to a linked list of all window objects. Wall methods are defined to enable operations common to all windows with only a single user command. Operations that can be performed by Wall include window redraws, turning logs on and off, supplying window information, and dumps to disk or printer.

WFI is written in Turbo Pascal v6.0 for IBM PC-series and compatible computers running MS-DOS. Turbo Pascal v6.0 or v7.0 (Borland) is required to compile the source code. Five demonstration executable codes with source code are provided on the distribution medium. These executable codes require at least 34K of random-access memory and DOS 3.1 or higher. The standard medium for distribution of this program is one 3.5-in. (8.89-cm), 1.44MB, MS-DOS-format diskette. An electronic copy of the documentation is provided in ASCII format on the distribution medium. WFI was developed in 1993.

This program was written by R. Katz of Goddard Space Flight Center. Further information is contained in a TSP [see page 1].
GSC-13632



Mechanics

Hardware, Techniques, and Processes

- 41 SR-71 Experiment on Propagation of Sonic Booms
- 42 Mechanism Attaches to Special Fixture
- 42 Assembling Precise Truss Structures With Minimal Stresses
- 44 Rod Has High Tensile Strength and Low Thermal Expansion

Books and Reports

- 44 Space-Suit-Sizing Device

BLANK PAGE

SR-71 Experiment on Propagation of Sonic Booms

Data will be used to soften sonic booms from supersonic aircraft.

Dryden Flight Research Center,
Edwards, California

A flight experiment was recently conducted at NASA's Dryden Flight Research Center in Edwards, California, using an SR-71, an F-16XL, and a YO-3A airplane (see Figure 1) to study the propagation of sonic booms. This work is geared toward developing a high-speed civil transport (HSCT) aircraft for operational use early in the next century.

At supersonic speed, an aircraft generates numerous shock waves that emanate from such major components as the nose, canopy, inlets, wings, and vertical tails. These multiple shock waves tend to merge into a strong bow shock and a strong tail shock as they propagate through the atmosphere. At present, supercomputers and wind tunnels are used to predict the structures of these shock waves, but only within a few body lengths of the aircraft. Other computational techniques are then used to determine the propagation and merging of these shock waves down to ground level. To verify and enhance the quality of these computational propagation techniques, a data base of sonic-boom measurements at various altitudes was gathered for use by the aerospace industry, universities, and NASA research centers. These organizations will use the enhanced computational techniques in the design of the HSCT. Varying the design of an HSCT could help soften the intensities of sonic booms at ground level.

In the experiment, an SR-71 (commonly known as the Blackbird) airplane, was used to generate the sonic booms. The SR-71 flew at speeds from mach 1.25 to 1.60, altitudes from 31,000 to 48,000 ft (9.4 to 14.6 km), and gross weights from 73,000 to 118,000 lbf (325 to 525 kN) in steady, level flight. The F-16XL flew below and behind the SR-71, probing in and out of the shock waves generated by the SR-71. Sensitive pressure transducers measured the pressure changes from these shock waves. By flying the F-16XL in formation with the SR-71, the spatial resolution of the shock wave measurements was maximized and the F-16XL gathered 105 probeings during only 7 flights. These probeings were measured from close to the SR-71 to more than 11,000 ft (2.4 km) below. Both aircraft carried differentially corrected carrier-phase Global Positioning System (GPS) receivers. Subtracting the position of the F-16XL from that of the SR-71



Figure 1. These Airplanes Were Used to gather data on sonic booms. From top to bottom, they are the SR-71, F-16XL, and YO-3A.

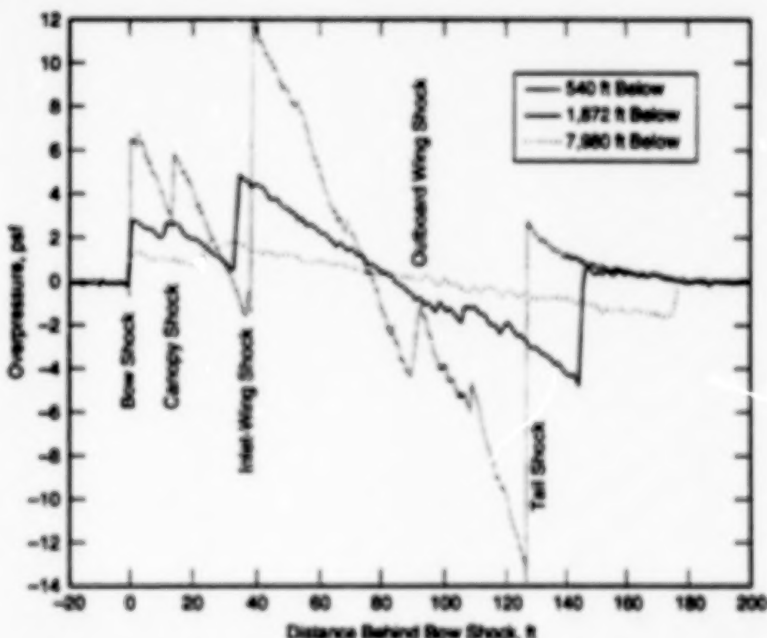


Figure 2. These Sonic-Boom Signatures are based on preliminary measurement data acquired by flying the F-16XL at several distances below the SR-71. The SR-71 was flying at mach 1.25 and an altitude of 31,000 ft (9.4 km).

gave relative position and distance with an accuracy on the order of 1 ft (0.3 m).

A large array of sonic-boom recorders was deployed on the ground under the

flight track of the SR-71 to measure the sonic-boom signatures. During eight SR-71 flights, 172 separate ground-level signatures were recorded. Sonic booms are

affected by temperature, wind, humidity, and turbulence as they propagate through the atmosphere. In particular, the turbulent atmospheric layer near the ground distorts the sonic-boom signatures. To provide undistorted data at low altitude, the low-speed YO-3A airplane was flown at an altitude of 10,000 ft (3 km) to record the sonic booms above the turbulent atmospheric layer. Sensitive microphones were located at each wing tip and at the tip of its vertical tail. The YO-3A recorded 17 passes of the SR-71. Sonic booms that had first been reflected from the ground and then

propagated upward to the YO-3A were also recorded. Atmospheric data were gathered for use in analysis of flight data and in computing codes for predicting the propagation of sonic booms. The flight-test techniques used in this experiment to measure pressures and relative aircraft separation accurately are also under consideration for use in other flight research unrelated to sonic booms.

Preliminary analysis of the data shows the attenuation and lengthening of the sonic boom signatures as they propagate through the atmosphere, as well as the

merging of individual shock components. The Mach number, altitude, and gross weight (which translates into lift) all affect the propagation characteristics. Analysis of the flight data and ground-recorded signatures continues, but preliminary results have been published in papers from the NASA High Speed Research Program's 1995 Sonic Boom Workshop.

This work was done by Edward A. Haering, Jr., of Dryden Flight Research Center. Further information is contained in a TSP [see page 1].
DRC-95-32

Mechanism Attaches to Special Fixture

Hooks and bumper pads hold the device in place.

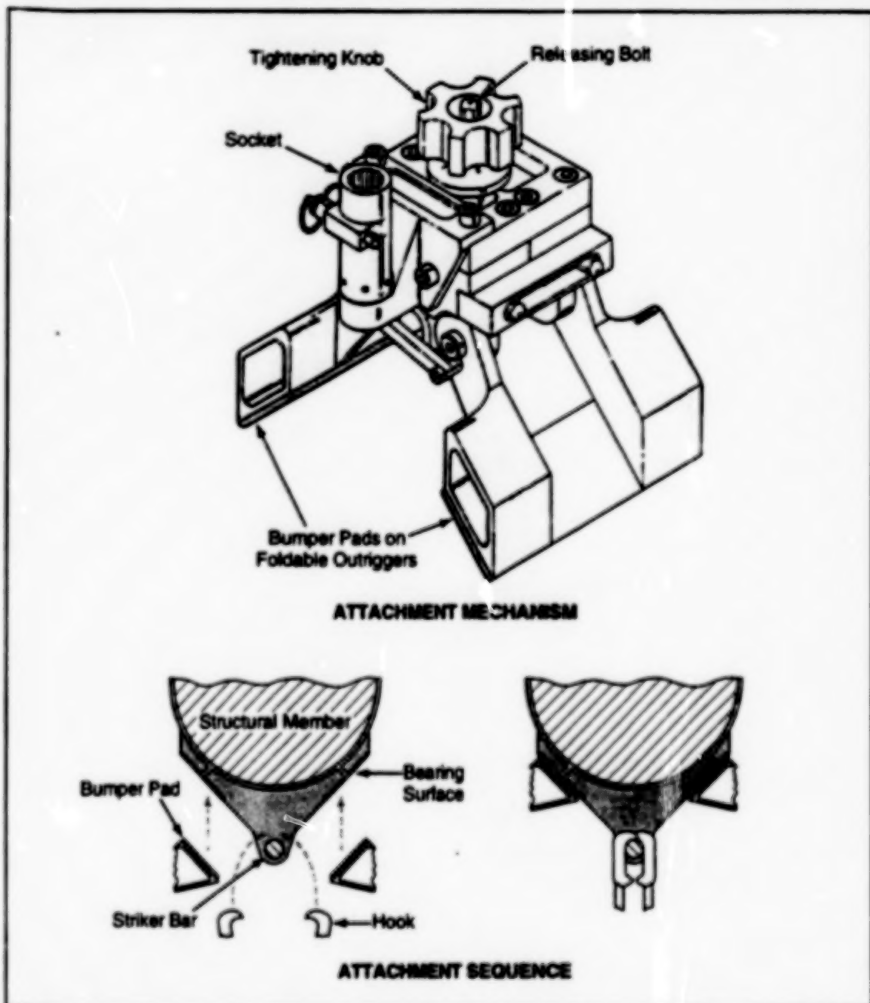
Lyndon B. Johnson Space Center, Houston, Texas

The figure illustrates a mechanism designed for attachment to a special fixture on a round structural member. In the original application, the special fixture is a striker bar, the round structural member lies at the end of a remote manipulator on the space shuttle, and the mechanism is used to attach a foot restraint for use by an astronaut during extravehicular activity. On Earth, similar mechanisms and fixtures with suitably modified dimensions might be useful for temporary attachment of various items (e.g., safety harnesses) to structures or machines.

The mechanism is initially brought into approximate alignment with the striker bar or other fixture. The knob on top of the mechanism is turned to pull the hooks into firm contact with the striker bar, thereby bringing the bumper pads into firm contact with the bearing surfaces on the structural member near the brackets that support the striker bar. The item to be attached to the structural member (the foot restraint in the original application) is attached via a socket in the mechanism.

This work was done by Ronald James Zaguli of Johnson Space Center. Further information is contained in a TSP [see page 1].

This invention is owned by NASA, and a patent application has been filed. Inquiries concerning nonexclusive or exclusive license for its commercial development should be addressed to the Patent Counsel, Johnson Space Center [see page 1]. Refer to MSC-21885.



The Attachment Mechanism grasps the striker bar with hooks, pulling itself inward so that its pads press against the structural member.

Assembling Precise Truss Structures With Minimal Stresses

Tapered pins that fit in tapered holes indicate deviations from prescribed lengths.

NASA's Jet Propulsion Laboratory,
Pasadena, California

An improved method of assembling precise truss structures involves the use of simple devices that indicate the devi-

ations of the lengths of members (distances between node points) from the prescribed lengths. The method both

helps to ensure the precision of the finished structures and to minimize residual stresses within the structures.

Previously, in the laboratory setting in which the method was devised, precision of a truss was enforced during assembly by securing selected node points of the truss to designated locations on a reference plate. Any residual compressive or tensile stresses in the members between node points were borne and thus hidden by the reference plate. Consequently, when the node points were released, these residual stresses were no longer resisted by the reference plate, and the structure became distorted.

In the improved method, the node points are not secured to a reference plate or to any other fixture that could temporarily resist and thus mask substantial residual structural stresses. In this method, conically tapered pins that are oriented facing downward are installed at measurement points on the nodes of horizontal members of the truss. Conical holes that mate with these pins are machined into a horizontal reference plate at positions that correspond to the precise design configuration of the horizontal truss members (see Figure 1). Similarly, tapered pins that face outward are installed at other measurement points on the nodes of nonhorizontal members of the truss. A reference bar that functions as a reference plate for the nonhorizontal members is made by machining conical holes at the precise design distances along a square-cross-section aluminum tube.

The horizontal members are assembled on the reference plate with node pins inserted in the conical holes. The pins are thus pushed gently into the holes by the weight of the structure, but are not otherwise forced into an alignment that places the members under substantial stresses. Similarly, the reference bar is held against the nodes at the ends of a nonhorizontal member, so that the pins are pushed gently into the mating holes (see Figure 2).

When the length of any member deviates from the design value by more than 0.005 in. (0.13 mm), the misalignment between the pin and hole at either or both ends of the member is clearly visible. The lengths of the members can be adjusted until the structure is in the required configuration, as indicated by alignment of all pins with their reference holes. Thereafter, the structure retains its precise configuration because unlike in the previous method, the completion

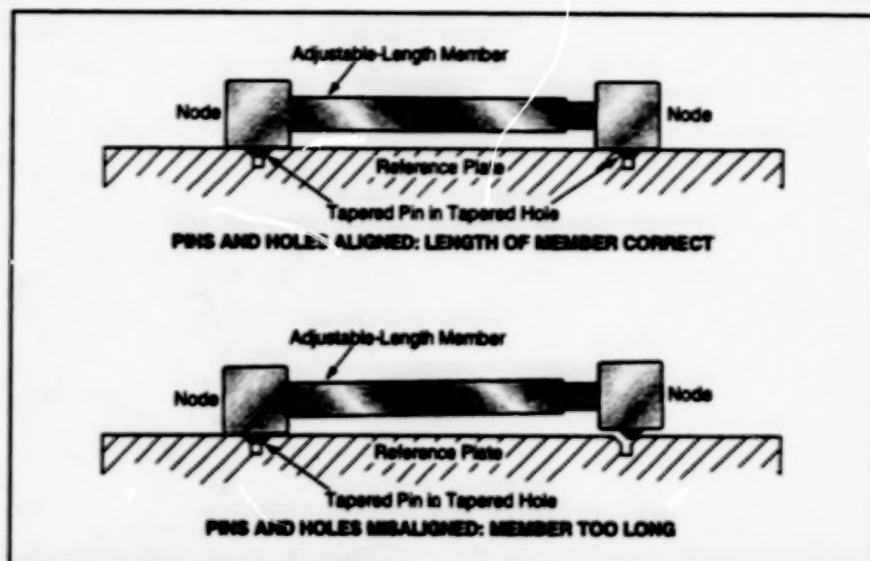


Figure 1. Misalignment Between One or More Pin(s) and Hole(s) is clearly visible as an indication that the length of the member deviates from the precise design value.



Figure 2. The Technician Holds the Reference Bar, which functions similarly to the reference plate shown in Figure 1.

of the assembly and alignment process does not involve a substantial alteration in the state of stress in the structure.

This work was done by Lee F. Sword of Caltech for NASA's Jet Propulsion

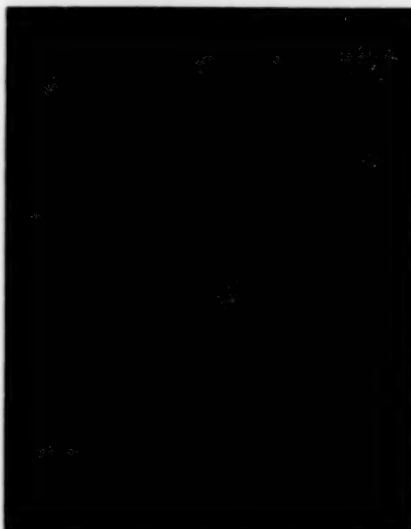
Laboratory. Further information is contained in a TSP [see page 1].
NPO-19114

Rod Has High Tensile Strength and Low Thermal Expansion

Thoriated tungsten is turned and threaded to form an extension rod for a gap gauge.

A thoriated tungsten extension rod has been fabricated to replace a stainless-steel extension rod attached to a linear variable-differential transformer in a gap-measuring gauge. The extension rod and adjacent parts of the gauge are required to withstand temperature as high as 1,000 °F (≈540 °C) and differential pressure as high as 2.2 kpsi (≈15 MPa). (In the original application, the gauge is used to measure a gap in a rocket motor.) Thoriated tungsten was chosen over stainless steel and other candidate rod materials because it offers a more nearly optimum combination of properties including, most notably, a low coefficient of thermal expansion [$2.5 \times 10^{-6}/^{\circ}\text{F}$ ($4.5 \times 10^{-6}/^{\circ}\text{C}$)], high tensile strength [590 kpsi (≈4.1 GPa)], nonmagnetism, and some ability to withstand shock accelerations.

The rod is made from thoriated tungsten TIG (Tungsten Inert Gas) welding-electrode stock 0.125 in. (≈3.2 mm) in diameter, containing 2 percent thoriated tungsten. The stock is held in a drill guide



Threads Are Formed on the end of the thoriated tungsten rod by machining with special fixtures and a carefully chosen combination of speeds and feeds.

on a lathe, where it is turned at a speed of 478 r/min, with a removal rate of 0.003 in. (≈0.08 mm) per revolution, to

machine it down to a diameter of 0.060 in. (≈1.5 mm). One end of the rod is then threaded (see figure) at 80 threads per inch (≈3.1 threads per millimeter). The threading operation is performed with the help of a special threading guide at a machine speed of 125 r/min, using a 90° end mill rotating at 400 r/min to form the notch, which is cut at 0.0005 in. (≈0.013 mm) per pass. Special care must be taken in these machining operations: small deviations from the recommended machining speeds and feeds cause shattering of the tungsten rod into several pieces.

This work was done by D. E. Smith, R. L. Everton, E. Howe, and M. O'Malley of Thiokol Corp. for Marshall Space Flight Center. Further information is contained in a TSP [see page 1].

Inquiries concerning rights for the commercial use of this invention should be addressed to the Patent Counsel, Marshall Space Flight Center [see page 1]. Refer to MFS-28891.

Books and Reports

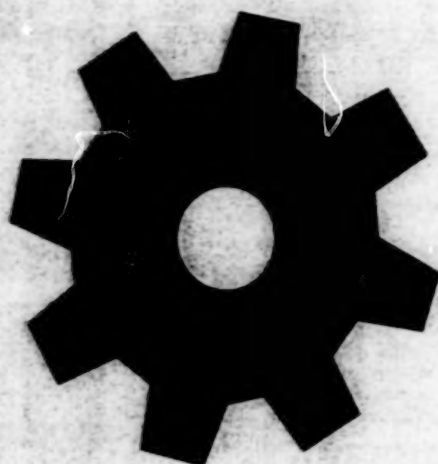
Space-Suit-Sizing Device

A report that consists of the main text of U. S. Patent 5,409,331 describes a device for adjusting the length of an arm or leg portion of a space suit to fit more than one astronaut. The device includes a stationary ring to which an inner impermeable layer of the suit is sealed, a short tube that is mounted on ball bearings in a circumferential groove on the stationary ring so that it can be turned freely, and an axially translatable (but not rotatable) ring attached to

outer layers of the suit. The outer portion of the translatable ring engages a thread-like groove on the inner surface of the rotatable tube via recirculating balls that travel in the groove, so that turning the tube causes the translatable ring to translate axially to lengthen or shorten the outer layers of the sleeve. As the affected portion of the suit is shortened or lengthened, the impermeable inner layer is simply folded into or withdrawn from the space between the inner surface of the tube and the astronaut's arm or leg.

This work was done by Hubert C. Vykukal of Ames Research Center. To obtain a copy of the report, "Space Suit Sizing Device," see TSP's [page 1].

This invention has been patented by NASA (U.S. Patent No. 5,409,331). Inquiries concerning nonexclusive or exclusive license for its commercial development should be addressed to the Patent Counsel, Ames Research Center [see page 1]. Refer to ARC-13377.



Machinery

Hardware, Techniques, and Processes

- 47 Jet-Engine Exhaust Nozzle With Thrust-Directing Flaps
- 48 High-Current Rotating Contactor
- 48 Aqueous-Spray Cleaning System

Books and Reports

- 48 Improvements in Ball-Screw Linear Actuators

BLANK PAGE

Jet-Engine Exhaust Nozzle With Thrust-Directing Flaps

Large attitude-control forces are produced, with minimal loss of performance.

Langley Research Center,
Hampton, Virginia

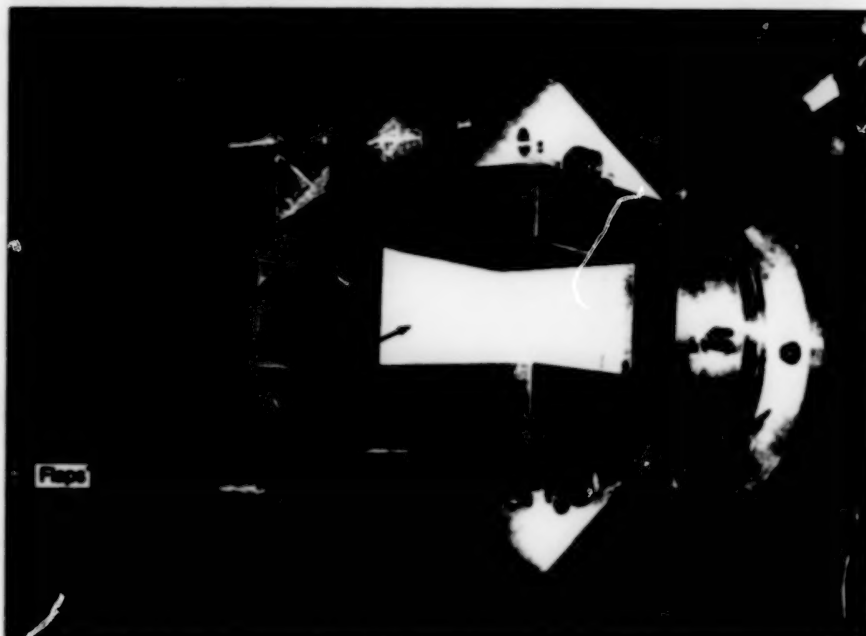


Figure 1. The Cruciform Nozzle is shown here mounted on a test stand, with the diverging flaps positioned symmetrically for "unvectored" (nondeflecting) operation.

An experimental convergent/divergent jet-engine exhaust nozzle has a cruciform divergent passage containing flaps that can be moved to deflect the flow of exhaust in either or both planes perpendicular to the main fore-and-aft axis of undeflected flow. This nozzle is a prototype of thrust-vector-control nozzles that would be installed in advanced, high-performance airplanes to provide large pitching (usually, vertical) and yawing (usually, horizontal) attitude-control forces independent of the attitude-control forces produced by the usual aerodynamic control surfaces. Other nozzles have been considered for this purpose in recent years, but their combined pitch/yaw thrust-vector capabilities have been limited by physical interference between flaps and by asymmetries.

The nozzle contains four sets of hinged convergent and divergent flaps positioned to form the top, bottom, left, and right sides of the nozzle. Four L-shaped corner pieces form channels within which the divergent flaps are moved to obtain the desired deflection (see Figure 1).

In the nondeflecting ("cruise" or "unvectored") mode of operation, the flaps are arranged symmetrically to form a convergent/divergent exhaust nozzle. In the single-axis deflecting ("thrust-vec-

toring") mode of operation (see Figure 2), the upper and lower (or the right and left) diverging flaps are both turned in the same direction to create a component of thrust in the vertical (or horizontal, respectively) plane of deflection. In the two-axis thrust-vectoring mode, both pairs of opposing flaps are deflected simultaneously to create both vertical and horizontal components of thrust. To prevent physical interference between adjacent flaps during large simultaneous deflections in both planes, the two pairs of convergent/divergent flaps for either the horizontal or the vertical plane are shifted laterally with respect to the main axis of the nozzle. This feature is essential to the capability to produce large, essentially equal components of thrust along both axes perpendicular to the main fore-and-aft axis.

In experiments, in the unvectored mode, the cruciform nozzle exhibited internal-thrust and mass-flow performances competitive with those of previous nozzles. The thrust performance of the cruciform nozzle with single-axis thrust vectoring was 1 to 2 percent lower than the thrust performances of other, comparable two-dimensional convergent/divergent nozzles; loss being attributed to splitting of the flow. Additional loss of thrust was observed in

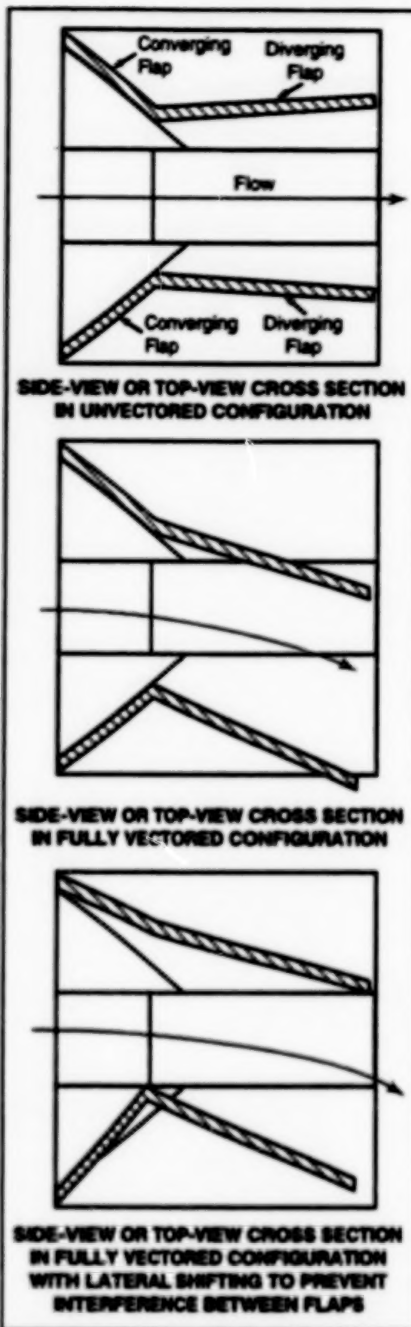


Figure 2. The Flaps Are Positioned and Oriented to control the direction of flow of the exhaust and thus the direction of thrust.

two-axis thrust vectoring, and was attributed to some turning of supersonic flow.

This work was done by David J. Wing of Langley Research Center. Further information is contained in a TSP [see page 1].
LAR-14692

High-Current Rotating Contactor

A rotating electrical contactor capable of carrying 1,000 amperes of current has been built for use in rotating a large workpiece in an electroplating bath. Electrical contact is made by use of 24 automotive starter motor brushes adapted to match the inside diameter of

a shell electrode. This contactor replaces a previous contactor in which current was conducted via a stationary electrode and a shell electrode via a mercury bath. After nearly 500 h of use, no signs of degradation of the contactor were observed.

This work was done by David W. Hagan and Edwin D. Wolff of Rockwell International Corp. for Marshall Space Flight Center. Further information is contained in a TSP [see page 1].
MFS-30063

Aqueous-Spray Cleaning System

A simple aqueous-spray cleaning system with overall dimensions comparable to those of a large kitchen refrigerator has been constructed for use in cleaning hardware in a shop. If mass-produced, the system would likely be competitive with similar currently available commercial aqueous-spray cleaning systems that are sold for about \$20,000

(1995 prices). The system is made of commercially available parts and materials; the only unusual major part is its spray cabinet, which contains spinner-type sprayers and is a surplus unit that was originally used for steam cleaning. The system incorporates an economical cleaner-and-rinse-recycling subsystem, as well as a programmable logic-con-

troller device for either manual or automatic operation.

This work was done by Gene E. Morgan, William S. Hout, and Gareth L. Simpson of Rockwell International Corp. for Marshall Space Flight Center. Further information is contained in a TSP [see page 1].
MFS-30074

Books and Reports

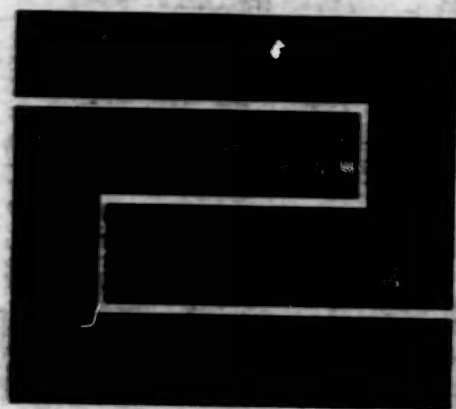
Improvements in Ball-Screw Linear Actuators

A report describes modifications of the design of a type of ball-screw linear actuator driven by a dc motor, with linear-displacement feedback via a linear variable-differential transformer (LVDT). The actuators are used to position spacecraft engines to direct thrust. Actuators of the original design were used on the Viking mission to Mars, and the modified design is intended to satisfy the more exacting requirements of the Cassini mission to Saturn. The modifications are directed toward ensuring reliable and predictable operation during a

planned 12-year cruise and an interval of hard use at the end of the cruise. The modifications included (1) reconfiguration and reorientation of the LVDT to eliminate flexing of its external wires and thus prevent breaking of the wires under cyclic stress; (2) incorporation of a flexure rod to reduce side loads on rubbing surfaces to minimize wear and wear debris; (3) addition of soft stops to cushion impact when the screw reaches the limits of its travel; (4) enlargement of the surfaces of antirotation sliders on the ball screw and repositioning these sliders at a larger radius to reduce loads and wear at their rubbing surfaces; (5) changing the motor magnet material and

reorienting the magnets to minimize the external magnetic field, power consumption, and heating; (6) addition of a grease reservoir to release lubricant to the ball screw as it is needed over time; (7) choice of motor brush and commutator materials to resist corrosion; and (8) general redesign to enable more tests of assemblies and sub-assemblies during the assembly process.

This work was done by Theodore Iskenderian, Benjamin Joffe, and Robert Summers of Caltech for NASA's Jet Propulsion Laboratory. To obtain a copy of the report, "Ball screw linear actuator," see TSP's [page 1].
NPO-10005



Fabrication Technology

Hardware, Techniques, and Processes

- 51 Ultrasonic Inspection of Welds on Tube Fittings
- 51 Push/Push Fastener
- 52 Adhesion Casting in Low Gravity

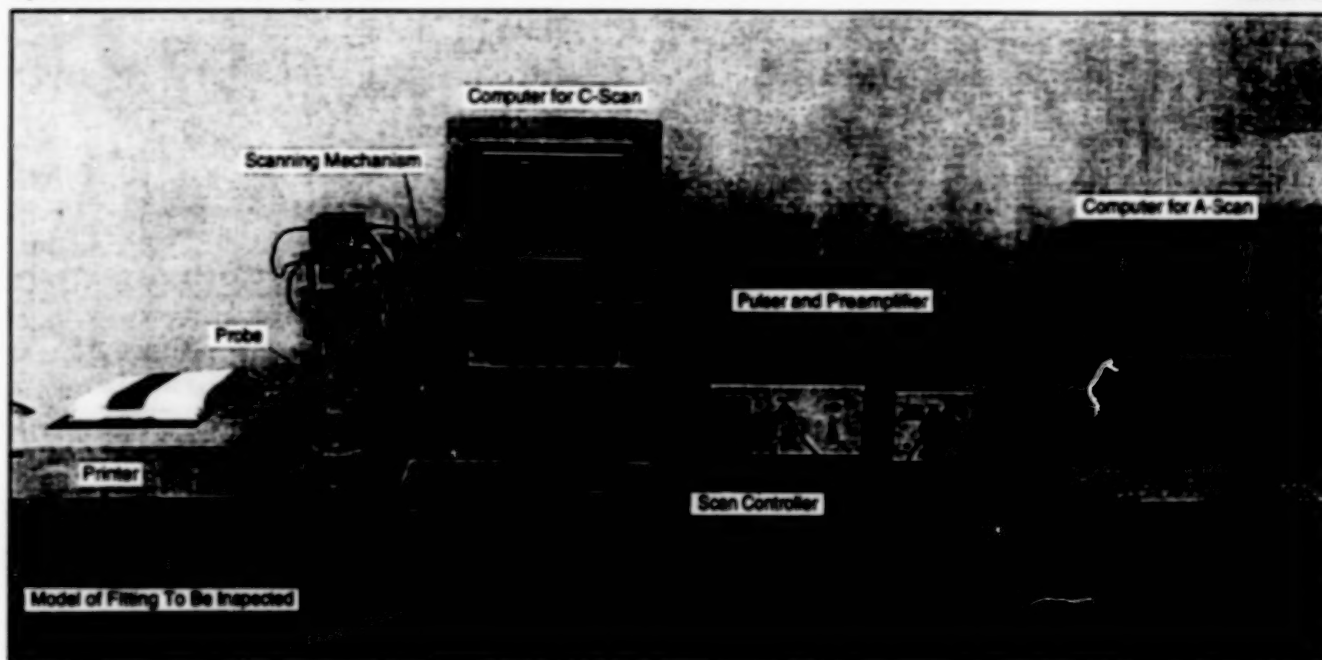
BLANK PAGE

50

Ultrasonic Inspection of Welds on Tube Fittings

An ultrasonic scanner is designed for the specific items to be inspected.

Marshall Space Flight Center,
Alabama



The Ultrasonic-Testing Apparatus is designed specifically for use in inspecting welds in tube fittings. The scanning mechanism is shown here attached to a model of a fitting on the table; in a real inspection, it would be attached to a fitting welded on the end of a tube.

A scanning ultrasonic apparatus is designed for use in nondestructive inspection of electron-beam welds between a heat-exchanger tube and its end fittings. The apparatus (see figure) includes an ultrasonic probe, a scanning mechanism, ultrasonic-signal-generating and -processing circuits, and computers. It is not necessary to immerse any part of the apparatus or tube/fitting assembly in water during the ultrasonic inspection.

The scanning mechanism is designed to be mounted on the fitting to be inspected. The mechanism inserts the probe axially into the fitting, rotates the probe 360°, and indexes the probe axially to scan the entire weld. The output ultrasonic-test signals can be displayed on a computer to reveal defects. To aid in identification of defects, signals obtained from the inspected fitting can be compared with those from a stan-

dard fitting that contains simulated defects in the form of notches and holes of various sizes. The scanning function provides data on the positions of flaws, which can then be reworked as needed.

This work was done by Arjun N. Ray and John L. Nummelin of Rockwell International Corp. for Marshall Space Flight Center. Further information is contained in a TSP [see page 1].
MFS-29848

Push/Push Fastener

Pushing from one side tightens the fastener; pushing from the other side loosens it.

Lyndon B. Johnson Space Center,
Houston, Texas

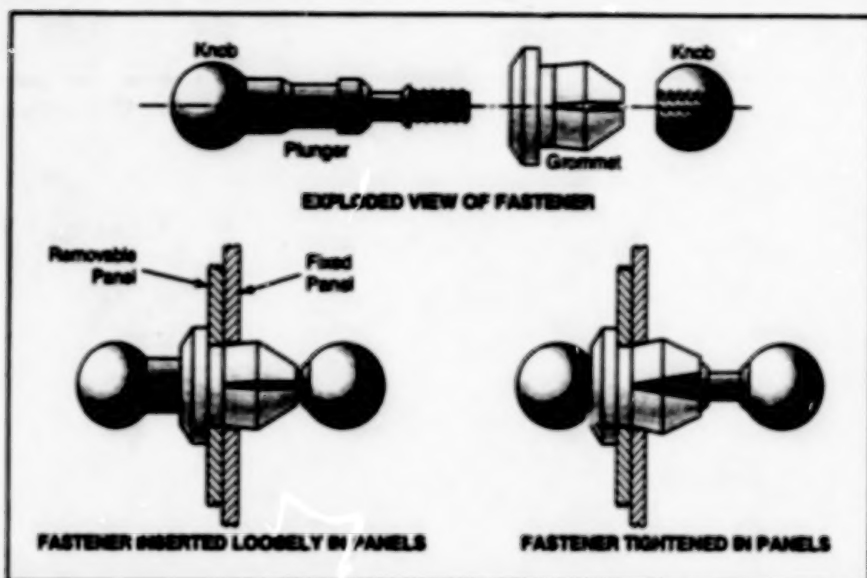
The figure illustrates a modified version of a Nylatch (or equivalent) commercial quick-connect/quick-disconnect fastener for joining flat panels. In the original version, the fastener is tightened or loosened by pushing or pulling, respectively, on a knob on one side (shown as left) of the joined panels. In the modified version, the fastener is tightened by pushing on the knob on one side and loosened by pushing on the knob on the other side.

The push/push operation of the modified fastener is advantageous because:

grasping and pulling a small knob can be difficult, especially in cold or otherwise hostile environments where gloves must be worn, in underwater operations, or if the person is handicapped. Of course, to be able to both tighten and loosen the modified fastener, one must have access to both sides.

Before the fastener is actually used to join the two panels, preliminary operations are performed: (1) Different sized holes are made in the panels to be joined; (2) The grommet is popped into the hole in the removable panel only; (3)

The threaded end of the plunger is inserted through the grommet and threaded into the right knob. The panels are put together by inserting the right knob through, and the grommet into, the hole in the fixed panel, thus providing a "soft dock." Note that the diameter of the right knob is slightly less than the diameter of the larger hole in the fixed panel. The dimensions of the holes, plunger, and grommet are chosen to provide a loose fit to accommodate any misalignments that might be present during insertion and before tightening.



The Modified Fastener is tightened by pushing the left knob rightward and loosened by pushing the right knob leftward.

To tighten the fastener, joining the panels securely, one pushes the left knob rightward (toward the panels), causing the plunger to expand the grommet against the edges of the hole in the fixed panel. To loosen the fastener, one simply pushes the right knob leftward (again, toward the panels).

This work was done by Steven A. Jackson of McDonnell Douglas Corp. for Johnson Space Center. Further information is contained in a TSP [see page 1].

This invention is owned by NASA, and a patent application has been filed. Inquiries concerning nonexclusive or exclusive license for its commercial development should be addressed to the Patent Counsel, Johnson Space Center [see page 1]. Refer to MSC-22329.

Adhesion Casting in Low Gravity

Stronger and lighter materials could be made.

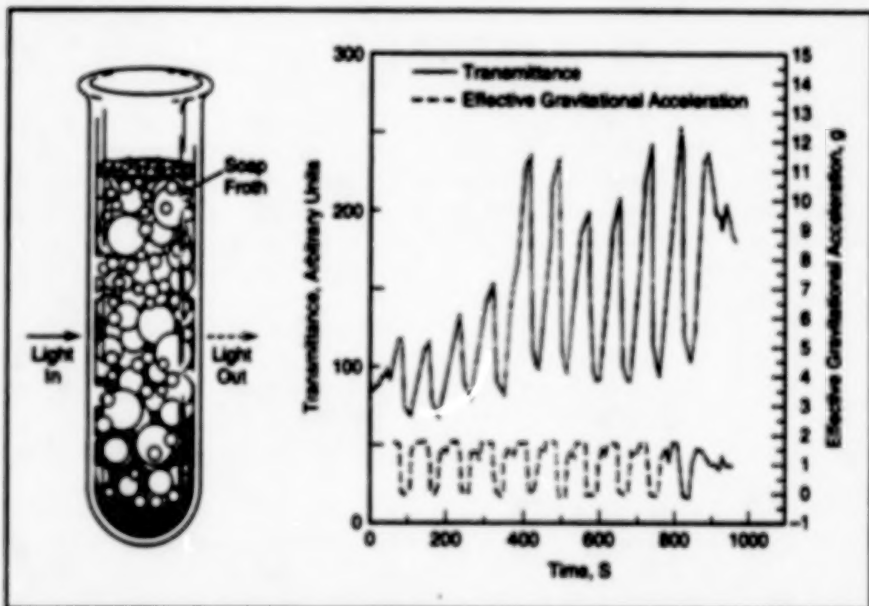
Marshall Space Flight Center, Alabama

Adhesion casting in low gravity has been proposed as a technique for making new and improved materials. The advantages of low-gravity adhesion casting, in comparison with adhesion casting in normal Earth gravity, would come from better control over, and greater uniformity of, the thicknesses of the liquid films that form on and adhere to solid surfaces during casting.

In low gravity, the magnitudes of capillary forces would be much greater than those of gravitational forces, so that capillary effects would be magnified. This enhancement of capillary action could be exploited to achieve more nearly uniform liquid coating on solid surfaces and/or more nearly uniform liquid impregnation of porous solids or beds of solid particles. It should be possible to exploit these effects to achieve greater strength-to-weight ratios in adhesion-cast materials.

A conceptual generic low-gravity adhesion-casting apparatus would include a controlled-temperature crucible and a reservoir of the liquid to be cast. A porous substrate, chemically compatible with the liquid, would be immersed in the liquid in the crucible, then removed with the liquid adhering to it. The liquid would then be polymerized or otherwise solidified by thermal, chemical, or optical means.

An experiment that demonstrated some of the relevant physical effects was performed in an airplane flying on repeating parabolic arcs to simulate low gravity



The Spectral Transmittance of the soap froth was measured along with the effective gravitational acceleration during cycles of alternating low and high simulated gravity. During low gravity, capillary forces predominated, causing the liquid to become more nearly evenly distributed in the foam. During high gravity, excess fluid was drained, resulting in coarsening of the foam, with consequent increase in the amount of light transmitted through the foam.

($\approx \pm 10^{-2}g$, where g = normal gravitational acceleration on the Earth) for about 25 seconds alternating with double Earth gravity ($2g$) for about 20 seconds and normal Earth gravity ($1g$) for about 20 seconds. In this experiment, a soap froth was used to illustrate the effects of capillary and gravitational forces (see figure).

This work was done by David A. Noever and Raymond J. Cronise of

Marshall Space Flight Center. Further information is contained in a TSP [see page 1].

Inquiries concerning rights for the commercial use of this invention should be addressed to the Patent Counsel, Marshall Space Flight Center [see page 1]. Refer to MFS-28906.



Mathematics and Information Sciences

Hardware, Techniques, and Processes

- 55 Fast Neural Solution of a Nonlinear Wave Equation
- 56 An Efficient Variable-Length Data-Compression Scheme

BLANK PAGE

Fast Neural Solution of a Nonlinear Wave Equation

The numerical solution by a simulated neural network closely approximates the exact solution.

NASA's Jet Propulsion Laboratory,
Pasadena, California

A neural algorithm for the simulation of a class of nonlinear wave phenomena has been devised. The algorithm numerically solves a special one-dimensional case of the Korteweg-deVries equation, which is a nonlinear wave equation that describes gravity waves like one-dimensional shallow water waves with finite amplitudes. The algorithm is intended to be executed rapidly by a neural network implemented as a charge-coupled-device/charge-injection device, very-large-scale integrated-circuit analog data processor of the type described in "CCD/CID Processors Would Offer Greater Precision" (NPO-18972), NASA Tech Briefs, Vol. 19, No. 10 (October 1995), page 38.

The special one-dimensional Korteweg-deVries equation in question is $u_t + 6uu_x + u_{xxx} = 0$, where u is the amplitude at time t and position x , and the subscripts represent partial differentiation with respect to the noted variables. This equation was chosen because its exact solution is known; therefore, one can determine the accuracy of the numerical solution produced by the neural network. The exact solution is

$$u(x,t) = 2k^2 \operatorname{sech}^2(kx - 4k^3t + \eta_0)$$

where k and η_0 are constants, with $k > 0$. This solution represents a solitary wave of amplitude $2k^2$ initially located at $x = -\eta_0/k$, moving with velocity $4k^2$.

The derivation of the algorithm begins with the reformulation of the special one-dimensional Korteweg-deVries equation into a discretized form with $2N$ points at equal intervals along the x axis, a pseudospectral (quasi-Fourier-transform) representation of the spatial dependence, and a leap-frog discretized approximation of the temporal derivative. The equation is reformulated further into a matrix-vector form suitable for computation on the CCD/CID neural network.

The heart of the neural network is a matrix of CCD/CID cells that performs matrix-vector multiplication. To recapitulate from the noted prior article: One of the gates of each cell is connected by a column electrode to the corresponding gates of all other cells in the same column. Similarly, another gate of the cell is connected by a row electrode to the corresponding gates of all other cells in the

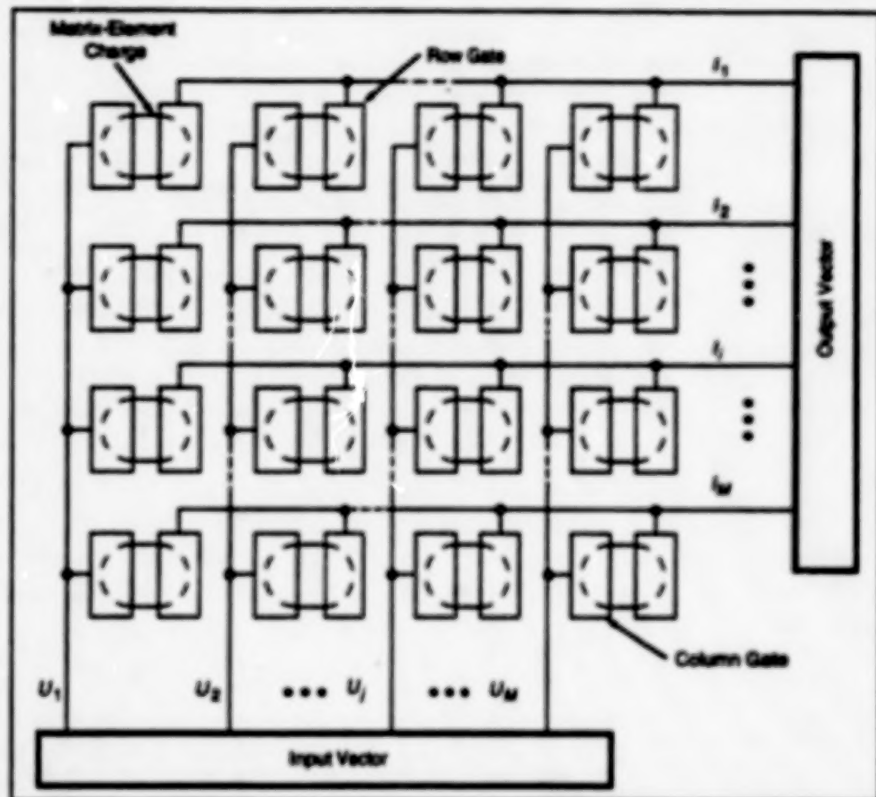


Figure 1. The CCD/CID Processor performs matrix vector multiplication in one clock cycle.

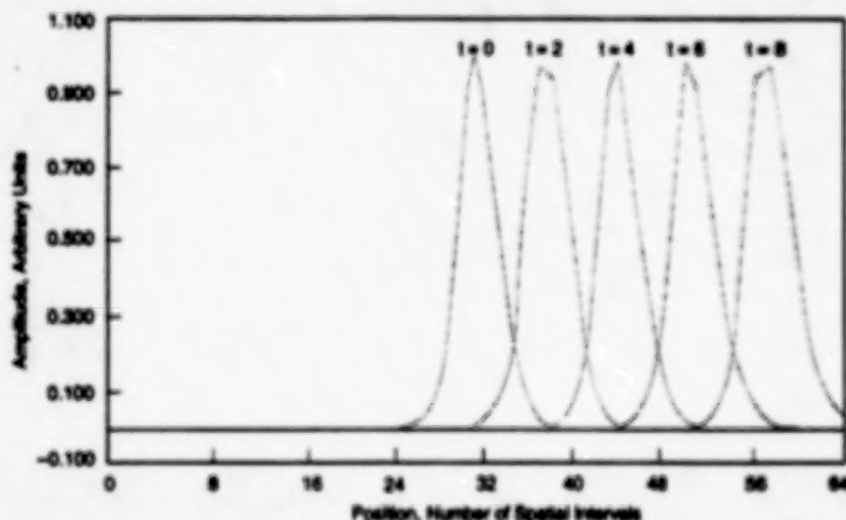


Figure 2. The Numerical Solution obtained by the neural simulation overlaps the exact solution so closely that one cannot distinguish the two solutions from each other on this plot.

same row. The charge stored beneath the row and column gates of each cell encodes the matrix element represented by the cell, while the column and row electrodes represent the input vector and the output vector, respectively. In its most basic configuration, shown in Figure 1,

such a circuit computes the product of a binary input vector and an analog matrix of charge. The computation done by each cell in the matrix is a multiplication and accumulation in which the matrix-element charge, Q_{ij} , is multiplied by a binary input vector element, U_j , encoded on the col-

umn line and this product is summed with other products in the same row to form I_j . Multiplication by a binary number is equivalent to adding or not adding the charge at a particular matrix element to its associated row line. Since all column electrodes are pulsed at the same time and the associated changes in voltage are then capacitively summed on the row lines in parallel, the entire matrix-vector multiplication is accomplished in one clock cycle. Many improvements have been incorporated into this basic structure, the most important being the ability to handle digital input and output. A prototype circuit of 256×256 elements is

expected to handle 10^{12} arithmetic operations per second per bit of precision.

Pending completion of the CCD/CID circuit, the neural algorithm was implemented as a computer program. For this purpose, the spatial region $[-20, +20]$ was divided into 64 intervals, and the initial condition (at $t = 0$) was chosen to be that of a solitary wave located at $x = 0$ and moving with a speed of 3.2 spatial intervals per unit time. The integration time step was chosen to be 0.005. As shown in Figure 2, the numerical results closely approximated the exact solution.

This work was done by Jacob Barhan and Nikzad Toomarian of Caltech for

NASA's Jet Propulsion Laboratory. Further information is contained in a TSP [see page 1].

In accordance with Public Law 96-517, the contractor has elected to retain title to this invention. Inquiries concerning rights for its commercial use should be addressed to

William T. Callaghan, Manager
Technology Commercialization
Jet Propulsion Laboratory
4800 Oak Grove Drive
Pasadena, CA 91109

Refer to NPO-18906 volume and number of this NASA Tech Briefs issue, and the page number.

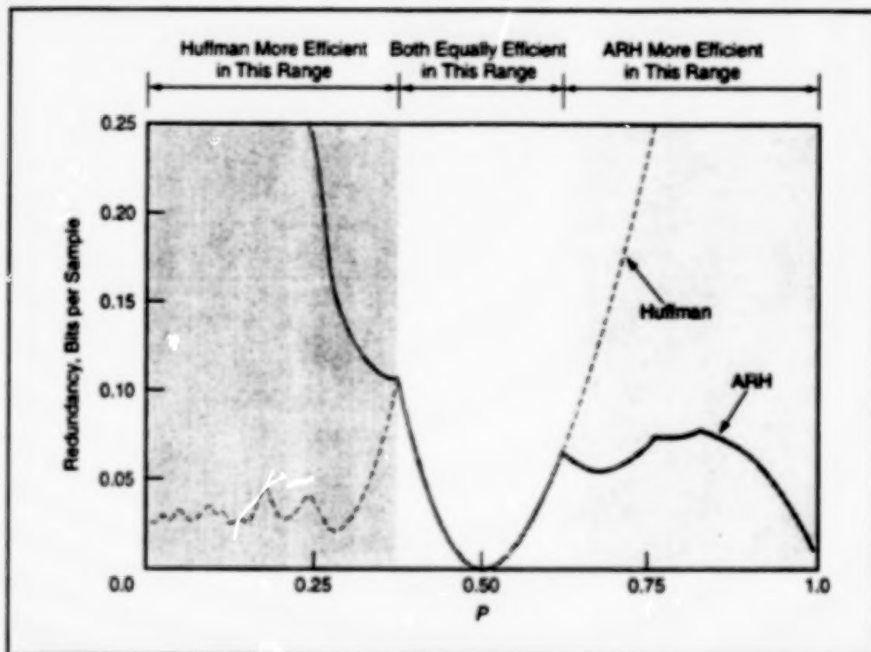
An Efficient Variable-Length Data-Compression Scheme

Either ARH or Huffman coding is chosen, depending on the characteristics of the data stream.

NASA's Jet Propulsion Laboratory,
Pasadena, California

An adaptive variable-length coding scheme for compression of a stream of independent and identically distributed source data involves the use of either a Huffman code or an alternating run-length Huffman (ARH) code, depending on the characteristics of the data. This scheme enables the efficient compression of the output of a lossless or lossy precompression process, with speed and simplicity greater than those of older coding schemes developed for the same purpose. In addition, this scheme is suitable for parallel implementation on hardware with a modular structure, provides for rapid adaptation to a changing data source, is compatible with block orientation to alleviate memory requirements, ensures efficiency over a wide range of entropy, and can be easily combined with such other communication schemes as those for containment of errors and for packetization.

The need for schemes of this type arises in connection with low-entropy sources. In a typical data-compression application, one data symbol often occurs much more frequently than others do. For example, in predictive coding, the error samples tend to be small, and in transform-based coding systems, the signal energy is usually more concentrated in the low-frequency components. In each of these cases, the data are quantized before compression, and the quantized data often constitute a low-entropy data source consisting of long runs of zeros interspersed with small nonzero values. The basic problem in this situation is how to achieve efficient coding of a low-entropy data source; that is coding at a rate less than 1 bit per sample. A well-known drawback of Huffman coding in this



The Redundancies of the Two Codes as functions of the probability (P) of occurrence of the most frequent symbol were calculated for a source in which the alphabet of code symbols is the set of nonnegative integers and the source statistics are characterized by the distribution probability $\{f_i\} = P(1 - P)^i$.

situation is that while the entropy may be near 0, the rate of a Huffman code can never be less than 1 because the Huffman code assigns a code word to every source symbol.

In an ARH code, one Huffman code represents the lengths of runs of the dominant symbol, while another Huffman code represents the remaining symbols. This run-length code enables the representation of the instances of the most frequent symbol using, on the average, less than one bit per sample. In ARH coding, the redundancy approaches zero as the probability (P) of

the most frequent symbol approaches 1.

In the present method, the choice of which code (Huffman or ARH) to use in a given application is dictated by a determination of which is more efficient, given the probability-of-occurrence characteristics of the data source. This determination can be made by use of the following four criteria derived from a theoretical analysis based on fundamental principles of Huffman coding:

1. If $P < 1/3$, then Huffman coding is more efficient.
2. If P lies between $1/3$ and $2/5$, then the efficiency of ARH coding is less than or

equal to that of Huffman coding, depending on the probability distribution of symbols in the data source.

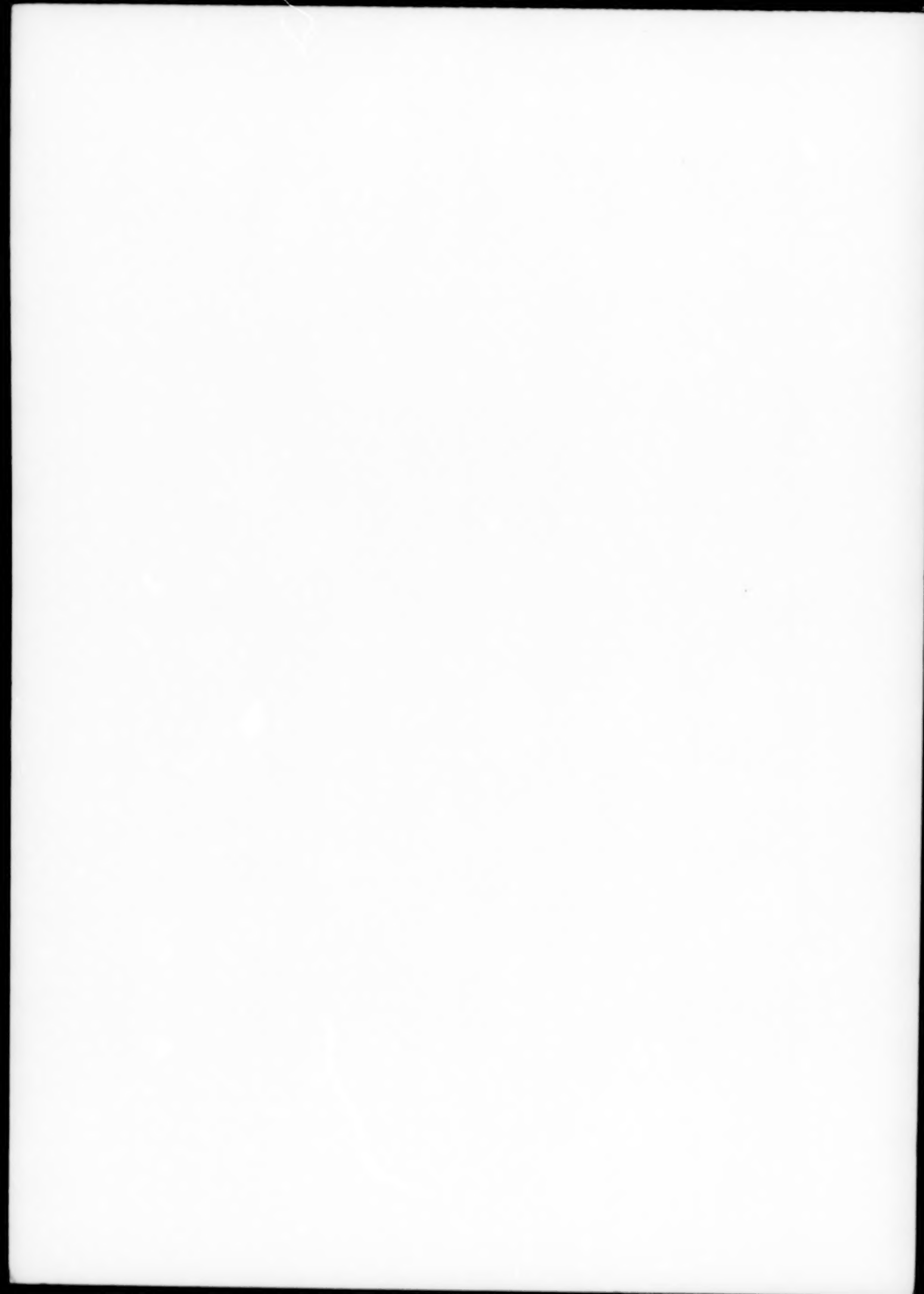
3. If P lies between $2/5$ and $(5^{1/2} - 1)/2$ [the reciprocal (≈ 0.618) of the "golden ratio" known since ancient times], then ARH

and Huffman coding are equally efficient.

4. If $P > (5^{1/2} - 1)/2$, then ARH coding is more efficient.

The figure illustrates the results of the theoretical analysis and application of the criteria to a test case.

This work was done by Ker-Ming Cheung and Aaron B. Kely of Caltech for NASA's Jet Propulsion Laboratory. Further information is contained in a TSP [see page 1].
NPO-19576



END

09-13-96